

Manuscript Number: NIMA-D-17-01100R1

Title: Position Resolution Simulations for the Inverted-coaxial Germanium  
Detector, SIGMA

Article Type: Full length article

Section/Category: Gamma, X-ray and Charged Particle Detectors

Keywords: Point contact germanium detector;  $\gamma$ -ray imaging;  $\gamma$ -ray  
tracking; Position sensitivity; Pulse shape analysis

Corresponding Author: Dr. Jonathan Paul Wright, Ph.D.

Corresponding Author's Institution: University of Liverpool

First Author: Jonathan Paul Wright, Ph.D.

Order of Authors: Jonathan Paul Wright, Ph.D.; Laura Harkness-Brennan;  
Andrew Boston; Daniel Judson; Marc Labiche; Paul Nolan; Robert Page;  
Fiona Pearce; David Radford; John Simpson; Carl Unsworth

Abstract: The SIGMA Germanium detector has the potential to revolutionise  $\gamma$ -ray spectroscopy, providing superior energy and position resolving capabilities compared with current large volume state-of-the-art Germanium detectors. The theoretical position resolution of the detector as a function of  $\gamma$ -ray interaction position has been studied using simulated detector signals. A study of the effects of RMS noise at various energies has been presented with the position resolution ranging from 0.33 mm FWHM at  $E_\gamma = 1$  MeV, to 0.41 mm at  $E_\gamma = 150$  keV. An additional investigation into the effects pulse alignment have on pulse shape analysis and in turn, position resolution has been performed. The theoretical performance of SIGMA operating in an experimental setting is presented for use as a standalone detector and as part of an ancillary system.

1 Position Resolution Simulations for the Inverted-coaxial  
2 Germanium Detector, SIGMA

3 J.P.Wright<sup>a</sup>, L.J.Harkness-Brennan<sup>a</sup>, A.J.Boston<sup>a</sup>, D.S.Judson<sup>a</sup>,  
4 M.Labiche<sup>b</sup>, P.J.Nolan<sup>a</sup>, R.D.Page<sup>a</sup>, F.Pearce<sup>a</sup>, D.C.Radford<sup>c</sup>, J.Simpson<sup>b</sup>,  
5 C.Unsworth<sup>a</sup>

6 <sup>a</sup>University of Liverpool, Oliver Lodge Building, Liverpool, L69 7ZE, UK

7 <sup>b</sup>STFC, Daresbury Laboratory, Daresbury, Warrington, WA4 4AD, UK

8 <sup>c</sup>Physics Division, Oak Ridge National Laboratory, Oak Ridge, TN 37831, USA

---

9 **Abstract**

The SIGMA Germanium detector has the potential to revolutionise  $\gamma$ -ray spectroscopy, providing superior energy and position resolving capabilities compared with current large volume state-of-the-art Germanium detectors. The theoretical position resolution of the detector as a function of  $\gamma$ -ray interaction position has been studied using simulated detector signals. A study of the effects of RMS noise at various energies has been presented with the position resolution ranging from 0.33 mm FWHM at  $E_\gamma = 1$  MeV, to 0.41 mm at  $E_\gamma = 150$  keV. An additional investigation into the effects pulse alignment have on pulse shape analysis and in turn, position resolution has been performed. The theoretical performance of SIGMA operating in an experimental setting is presented for use as a standalone detector and as part of an ancillary system.

10 *Keywords:* Point contact germanium detector,  $\gamma$ -ray imaging,  $\gamma$ -ray  
11 tracking, Position sensitivity, Pulse shape analysis

---

## 12 **1. Introduction**

13 The primary aim of the SIGMA (Segmented Inverted-coaxial GerMAanium)  
14 project is to demonstrate  $\gamma$ -ray tracking and imaging using point contact  
15 High Purity Germanium (HPGe) technology. SIGMA will be the first p-type  
16 segmented inverted-coaxial germanium detector to be manufactured. A sim-  
17 ilar large volume n-type HPGe detector utilising point contact technology  
18 was proposed in 2011 (1) with a working prototype currently being studied  
19 at Lawrence Berkeley National Laboratory (2).

20 One of the long term objectives is that detectors of this type could be  
21 deployed as part of the DEGAS HPGe array required for the DESPEC (DE-  
22 cay SPECTroscopy) experiment (3) at FAIR (Facility for Anti-proton and  
23 Ion Research). Additionally, this detector would be ideally suited for use as  
24 a single detector  $\gamma$ -ray imaging device for commercial and industrial appli-  
25 cations, enhancing performance in areas such as nuclear decommissioning,  
26 security, environmental monitoring and medical imaging.

27 One of the many benefits of using a point like contact is the reduced  
28 capacitance ( $\sim 1$  pF) of the electrode when compared to that of a standard  
29 coaxial detector ( $\sim 10$ 's of pF); a result of the reduced physical size of the  
30 contact. As a consequence, the signals from the point contact will exhibit  
31 extremely low series noise resulting in energy resolving capabilities superior  
32 to the current state-of-the-art large volume, segmented germanium detectors,  
33 an effect which is magnified at low energies. The energy resolution of a similar  
34 p-type Broad Energy Germanium (BeGe) detector was measured to be 0.5  
35 keV at a  $\gamma$ -ray energy of 59.5 keV and 1.7 keV at an energy of 1332 keV (4).

36 The pulse shapes from the detector preamplifier are significantly altered

37 from that of a standard coaxial detector due to the unique electrode config-  
38 uration and inverted-coaxial design. The chosen configuration increases the  
39 charge collection time and creates a complex relationship between drift time  
40 and  $\gamma$ -ray interaction position. Using digitised charge pulses, in addition to  
41 pulse shape analysis (5) techniques, the interaction position is predicted to  
42 be localised to  $<1 \text{ mm}^3$  throughout the detector volume, up to 5 times better  
43 than obtained in current state-of-the-art large volume HPGe detectors such  
44 as AGATA (6) and GRETINA (7). This combination of energy and position  
45 resolution has the potential to improve the performance of  $\gamma$ -ray tracking and  
46 imaging algorithms which utilise the  $\gamma$ -ray interaction position and energy  
47 to kinematically reconstruct their paths.

## 48 2. Detector Design and Characterisation

49 The dimensions of the SIGMA crystal are illustrated in Figure 1, with  
50 the point contact being referred to as the rear of the detector. The crystal  
51 measures 70 mm maximum diameter by 80 mm length, with a taper reducing  
52 the radius of the crystal to 24.5 mm at the front face. The taper starts 20  
53 mm from the rear of the crystal and tapers uniformly to the front face at  
54 an angle of  $10^\circ$ . The core measures 10 mm in diameter and extends 55  
55 mm into the bulk. The core, also known as a bore hole, enables large volume  
56 detectors to reach full depletion at a few thousand volts. The 6 mm diameter  
57  $\text{p}^+$  point contact is surrounded by a passivation region extending from  $r = 3$   
58  $\text{mm} \rightarrow r = 12 \text{ mm}$  as shown in blue in Figure 1.

59 The electrical segmentation scheme of the DC coupled outer contacts  
60 consists of 8 longitudinal rings, 2 concentric segments on the front face, 8

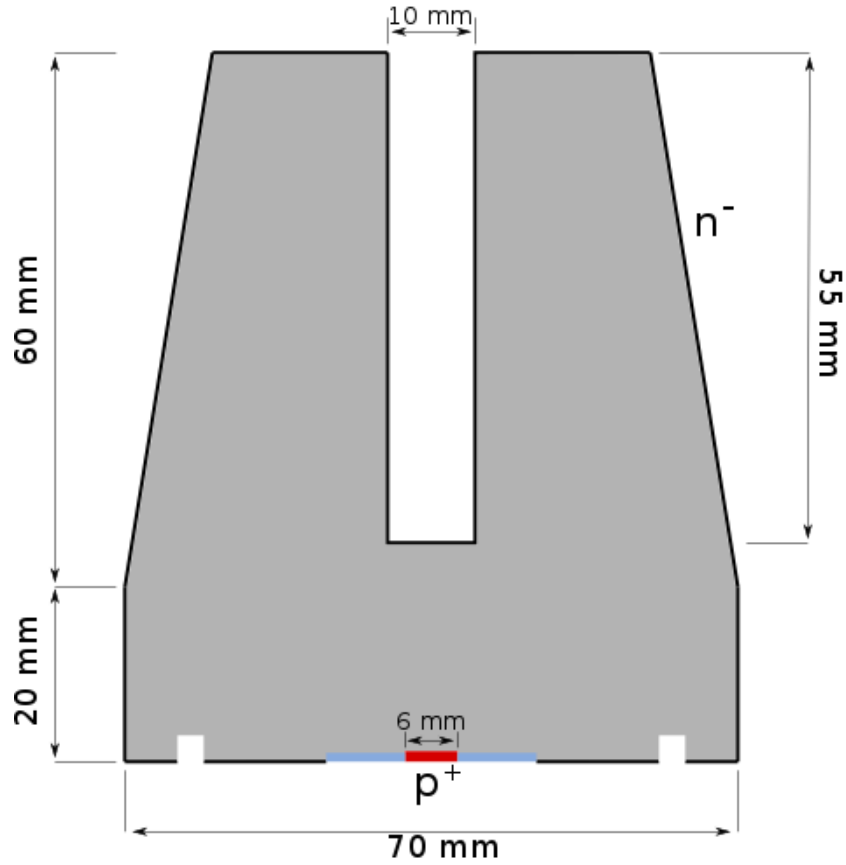


Figure 1: The SIGMA detector illustrating the dimensions of the crystal with the point contact shown in red (colour online).

61 azimuthal sectors, 1 core segment and a point contact on the rear face. Elec-  
 62 trons will be collected by the 19 segments, with the holes being collected at  
 63 the point contact. An illustration of the segmentation scheme is provided in  
 64 Figure 2. The discussion will refer to a cylindrical coordinate system,  $(r, \varphi, z)$ ,  
 65 where  $r$  is the radial distance from the central axis,  $\varphi$  is the angle around the  
 66 central axis and  $z$  is the distance from the rear of the crystal perpendicular  
 67 to  $r$ , with the centre of the point contact being  $(r, z) = (0, 0)$ . The angle

68  $\varphi$  is defined with  $\varphi = 0^\circ$  being the start of segment 1 and rotating around  
69 the segments in order. The 8 azimuthal segments provide angular informa-  
70 tion ( $\varphi$ ), with the longitudinal rings used to resolve the depth of interactions  
71 ( $z$ ). The addition of the front face segments and the core segments aid in  
72 resolving the radial position ( $r$ ) of the  $\gamma$ -ray interaction. From hereon, the 8  
73 azimuthal segments will be referred to as segments 1-8, with segments 9-16  
74 being the 8 longitudinal rings. The 2 concentric rings on the front face make  
75 up segments 17 and 18, with segment 19 being the core segment. The de-  
76 tector is currently being manufactured by MIRION TECHNOLOGIES. The  
77 impurity profile of the crystal has been measured by the manufacturer to be  
78  $1.02 \times 10^{10} \text{ cm}^{-3}$  at the rear of the detector, with an impurity of  $0.87 \times 10^{10}$   
79  $\text{cm}^{-3}$  at the front face of the crystal. This results in an impurity gradient of  
80  $-1.88 \times 10^8 \text{ cm}^{-4}$ , assuming a linear impurity gradient. The results presented  
81 are based on simulated work using these values and the physical dimensions  
82 described above.

### 83 *2.1. Field Simulations*

84 Simulations have been performed to calculate the electric and weighting  
85 potentials for SIGMA using a geometric adaptation of the FieldGen software  
86 developed at Oak Ridge National Laboratory (8). These simulations are cru-  
87 cial for calculating the drifts of charge carriers produced following a  $\gamma$ -ray  
88 interaction as they move through the crystal and measuring the expected re-  
89 sponse on each electrode. This software, along with the SigGen software (8),  
90 are established codes used for various experiments including GRETINA and  
91 MAJORANA. Simulations were initially performed to predict the voltage at  
92 which the detector fully depletes, with the results indicating full depletion

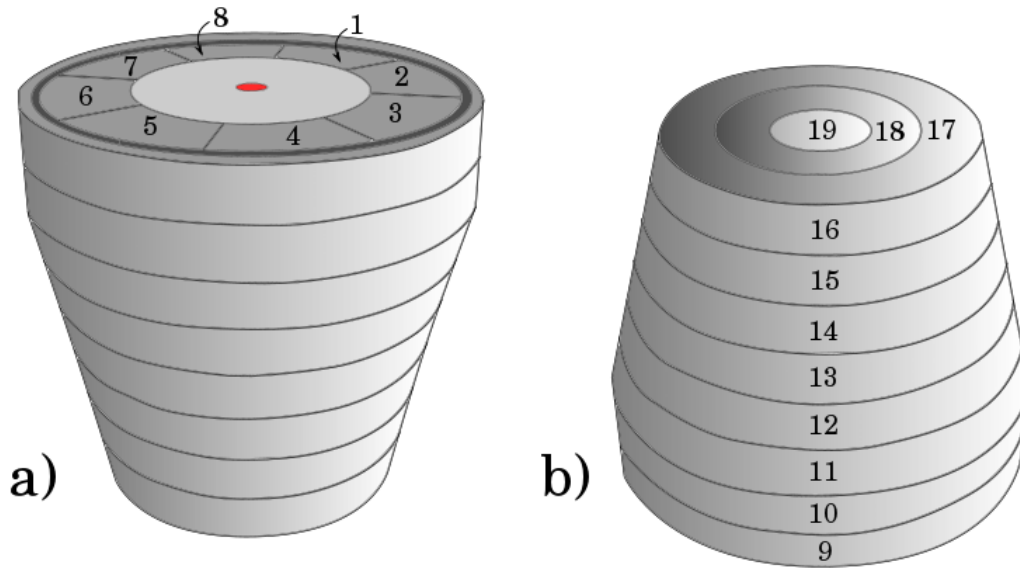


Figure 2: Schematic diagrams of the SIGMA detector showing the segmentation scheme with (a) and (b) showing the rear and front face of the crystal respectively. The point-like contact is coloured in red for illustrative purposes (colour online).

93 at -2000 V. Based on measurements made by the manufacturer, the recom-  
 94 mended operational voltage was set at -3000 V. The electric potential and  
 95 electric field strength for the SIGMA detector as a function of position have  
 96 been calculated. Parameters included in the simulation were the operating  
 97 voltage, detector geometry and electrode geometry. The results are shown  
 98 for  $\varphi = 0^\circ$  in Figure 3. The high voltage is applied directly to the point  
 99 contact, with the outer DC coupled contacts being grounded. Figure 3a  
 100 shows the short range of the electric potential, with the voltage reducing by  
 101  $\sim 50\%$  within 10 mm of the point contact. Figure 3b shows the electric field  
 102 strength, which is the gradient of the electric potential at each point in the  
 103 crystal. As can be seen, the field strength is very low for most of the detector,

104 which when combined with long charge drift paths of the holes to the point  
105 contact, will result in very long drift times of up to  $2\mu\text{s}$ .

106 The concept of a weighting potential (9; 10; 11) is used to calculate the  
107 instantaneously induced charge,  $Q$ , on an electrode, where

$$Q = q\Delta\varphi_0 \quad (1)$$

108 where  $q$  is the charge of the charge carriers and  $\Delta\varphi_0$  is the change in the  
109 weighting potential. This enables theoretical detector signals to be produced.  
110 Therefore, the weighting potential has been calculated for the point contact,  
111 see Figure 4a and for each segment, examples of which are shown in Figure 6.  
112 Due to the rotational symmetry of the detector, only 1 weighting potential  
113 is calculated for the azimuthal segments on the rear of the detector. This  
114 potential is then used for all 8 segments.

## 115 *2.2. Charge Transport Simulations*

116 The SigGen (8) software has been used to track charge produced follow-  
117 ing a  $\gamma$ -ray interaction throughout the detector. Inputs to SigGen include  
118 the fields calculated by FieldGen, polarity, crystal temperature, detector im-  
119 purity profile and the crystal lattice orientation. The electron drift velocity  
120 varies significantly as a function of temperature and crystallographic axis,  
121 with the crystallographic axis affecting the distance between atoms along  
122 the electric field lines changing for each orientation (12). In the simulation,  
123 charge is sampled as it drifts through the electric field at a frequency of 1  
124 GHz, equating to a 1 ns sample size for the resulting charge pulses. For  
125 consistency, the 1 GHz pulses are downsampled to 100 MHz to match the

126 sampling frequency that will be used by the digitiser cards for all experimen-  
127 tal measurements, with each result comprising 200 samples.

128 The weighting potential is responsible for the shape of the charge pulses,  
129 with the point contact potential, Figure 4a, showing virtually zero potential  
130 throughout the detector followed by a large rise near to the contact. This  
131 short range potential is reflected in the resulting charge pulses, with a sharp  
132 rise in the pulse amplitude as the charge carriers near the point contact.  
133 Two example pulses are shown in Figure 4b, with the red and green cir-  
134 cles in Figure 4a representing the  $\gamma$ -ray interaction positions corresponding  
135 to the red (solid) and green (dotted) pulses presented in 4b. This clearly  
136 demonstrates the temporal variation in the point contact pulse as a function  
137 of  $\gamma$ -ray interaction position. Due to this sharp rising edge, it is much easier  
138 to differentiate multiple interactions than in a comparable coaxial detector.  
139 Figure 5 shows all signals produced following a multi site event, with the  
140 point contact trace shown in red, the secondary collecting electrodes shown  
141 in green and the image charges highlighted blue. The point contact trace  
142 clearly shows 3 distinct rises followed by a plateau. This ability to distin-  
143 guish multiple site events is one of the major advantages of a detector such as  
144 SIGMA over current large volume HPGe detectors. The difference in pulse  
145 quality can be seen in Figure 5 with comparative pulses for AGATA available  
146 in (13). By comparing the point contact signal to the secondary charge col-  
147 lecting electrodes, the reduced clarity is clear to see, with the larger physical  
148 size of the outer segments being more representative of the response seen  
149 in a standard coaxial detector. Figure 6 shows the weighting potentials for  
150 four example segments with the increased size of the electrode responsible

151 for the increased spread in the weighting potential when compared with the  
152 point contact, Figure 4. This results in signals being induced on the contact  
153 at a much greater distance from the contact and explains the gradual slope  
154 in the charge pulses as opposed to the sharp rise seen in the point contact  
155 trace. The image charges (blue) shown in Figure 5 are a direct result of  
156 charge carriers passing through the weighting potentials of each electrode as  
157 they travel to their terminating electrode. This variation in the weighting  
158 potential causes a current to be induced on the electrode with the net charge  
159 returning to zero for non terminating electrodes.

### 160 *2.3. Drift Time Distributions*

161 Pulses provided by SigGen contain exact information regarding the start-  
162 ing time of the traces. The drift time as a function of position has been  
163 calculated as the time taken for the trace to rise from  $0 \rightarrow 95\%$  of the pulse  
164 height. The drift time calculated as a function of  $(r, z)$  is presented in Fig-  
165 ure 7a, with the top and bottom halves showing the distribution at  $\varphi = 0^\circ$   
166 and  $\varphi = 45^\circ$  respectively. For this discussion, only the drift time measured  
167 on the point contact is considered.

168 This plot shows a very strong relationship between  $z$  position and drift  
169 time in the front of the detector,  $\sim 25 < z < 80$  mm. In the rear of the  
170 crystal, the isochrone lines rotate and the direction of the gradient changes  
171 from longitudinal to radial. The variation between the two halves is due to  
172 the change in the crystallographic axis as a function of  $\varphi$  and can be seen more  
173 clearly in Figure 7b, which shows the variation in drift time as a function of  $\varphi$   
174 for a  $\gamma$ -ray interaction at  $(r, z) = (20, 20)$  mm. A clear oscillating behaviour  
175 is seen as the crystallographic axis varies as a function of  $\varphi$ , with a variation

176 of  $\sim 6\%$  seen in the drift time.

177 To understand the drift paths of the electrons in this detector, the elec-  
178 tron collecting electrode, outer hit segment, is plotted as a function of  $\gamma$ -ray  
179 interaction position in Figure 8. The relative sizes of each of the segments in  
180 Figure 8 are a direct result of the relative strengths of the weighting poten-  
181 tials shown in Figure 6 and provide a clearer image of the relative influence  
182 each electrode has on the charge collection path. The scale of the core contact  
183 is clear to see, with most interactions occurring near the central axis of the  
184 crystal terminating on the core. However for interactions occurring far from  
185 the central axis of the detector, there are clearly defined bands representing  
186 each of the outer contacts.

### 187 **3. Position Sensitivity**

188 The performance of tracking and imaging algorithms hinge on accurate  
189 measurement of  $\gamma$ -ray interaction energies and positions (14). With the ex-  
190 cellent energy resolution of HPGe point contact detectors, the success of  
191 SIGMA as a tracking and imaging detector will depend on the position reso-  
192 lution attainable. To study this, simulated signals have been generated and  
193 processed through a grid search algorithm to reconstruct the initial  $\gamma$ -ray  
194 interaction position. The grid search algorithm utilises a simple  $\chi^2$  min-  
195 imisation technique based on comparison between the charge pulses and a  
196 simulated pulse shape database; more detail is provided in section 3.1. A  
197 pulse shape database contains simulated charge pulses as a function of po-  
198 sition for use in pulse shape analysis, with the database used in this work  
199 having a grid size of 1 mm x  $3^\circ$  x 1 mm on a  $(r, \varphi, z)$  grid. As expected,

200 the grid search algorithm perfectly reproduces the  $\gamma$ -ray interaction posi-  
 201 tion when using the pulses directly generated from SigGen. In a laboratory  
 202 environment, sources of noise and processing errors are introduced into the  
 203 charge pulses. Examples of these effects, such as electronic noise and pulse  
 204 alignment error, have been added to the simulation, with the effects of each  
 205 on the final position resolution calculated.

### 206 *3.1. Position Reconstruction*

207 A grid search (GS) algorithm has been used to reconstruct the  $\gamma$ -ray  
 208 interaction position. Tests were performed to study the most effective method  
 209 of calculating the  $\chi^2$ , in terms of both performance and time, where  $\chi^2$  was  
 210 calculated as

$$\chi^2 = \sum_{i,j} |S_{i,j}^m - S_{i,j}^s|^2 \quad (2)$$

211 where  $S_{i,j}^m$  and  $S_{i,j}^s$  represent the modified and simulated pulses summed over  
 212 the number of segments,  $i$ , and the number of samples,  $j$ . For the  $\chi^2$  study,  
 213 three sets of search parameters, GS 1  $\rightarrow$  GS 3, were tested, with each set  
 214 defined as

- 215 • GS 1  $\rightarrow$  Point contact + core + hit segment
- 216 • GS 2  $\rightarrow$  GS 1 + 8  $\times$  azimuthal segments
- 217 • GS 3  $\rightarrow$  All 19 segments + point contact

218 where the hit segment is defined as the electrode on which the electrons  
 219 terminate. Since the size of the charge cloud is not accounted for in these

220 simulations, there is no charge sharing and so there is only 1 hit segment for  
221 a single interaction. For the case when the electrons terminate on the core  
222 or one of the 8 azimuthal segments, the algorithm discards the ‘hit segment’  
223 trace from the calculation to prevent double counting.

224 For the study, a simulated pulse is taken for a single position, with a  
225 random Gaussian noise added to each sample to simulate the electronic noise,  
226 defined by the root mean square (RMS). The  $\chi^2$  is then calculated against  
227 each pulse in the basis, with the lowest value of  $\chi^2$  taken as the most likely  
228 interaction position. The difference between the known interaction position  
229 and the measured position is then recorded. This process is repeated for  
230 each position in the detector on a  $1 \text{ mm} \times 1 \text{ mm} \times 3^\circ$  grid. For this work  
231 to be valid, all knowledge of the input pulse must be unknown prior to the  
232 grid search. Since all of the effects added to the pulses are based on random  
233 distributions, this condition holds true and all post processing is done with  
234 no knowledge of the initial pulse.

235 To simulate the electronic noise, a random Gaussian distributed noise was  
236 added to each sample in the chosen pulse. Based on experimental measure-  
237 ments from a BEGe detector (4), the electronic noise was measured to be  $\sim 1$   
238 mV peak-to-peak. For white noise, the relationship  $V_{rms} = 6.6 \times V_{pp}$  holds  
239 true such that only 0.1% of the time, the RMS noise,  $V_{rms}$ , will exceed the  
240 nominal peak-to-peak value,  $V_{pp}$ , (15), giving a typical RMS noise of 0.15  
241 mV for the point contact. When processed through a typical 100 mV/MeV  
242 charge sensitive preamplifier, the average noise is  $\sim 1.5$  keV which gives a  
243 normalised RMS noise of  $\sim 1\%$  when assuming a  $\gamma$ -decay of  $E_\gamma = 150$  keV  
244 and  $2\%$  at 75 keV. For the study using normalised pulses, the value of  $2\%$  at

245 75 keV was used as the standard deviation to demonstrate the performance  
246 capabilities at low energies, with the mean centred at 0. For this initial study,  
247 the RMS noise was set to be equal on all segments, with a more realistic ap-  
248 proach to segment noise applied in section 3.2, where the effects of varying  
249 RMS noise is discussed in more detail.

250 The results are presented numerically in Table 1, showing the average  
251 variation in search time in addition to the deviation from the known position  
252 for  $\varphi$ ,  $r$  and  $z$ . The results clearly show that the mean deviation for all 3  
253 parameters decrease significantly from GS 1  $\rightarrow$  GS 2 with a smaller change  
254 occurring from GS 2  $\rightarrow$  GS 3. In addition, the time taken to search a single  
255 position increases more than 10 fold from GS 1  $\rightarrow$  GS 3. The major difference  
256 between the results arises from the improved reconstruction of the  $\varphi$  value,  
257 with the azimuthal segments containing much of the angular information.  
258 To remove the effects of a bad measurement, each position was simulated 10  
259 times, with the average deviation presented.

260 The  $\varphi$  improvement from GS 1  $\rightarrow$  GS 2 can be accounted for by the  
261 addition of extra azimuthal information. However, the improvement in  $r$   
262 and  $z$  resolution arises because the weighting potential for the core segment  
263 is so large that there exists a significant probability that the core segment  
264 is also the hit segment. In this scenario, the GS 1  $\chi^2$  is calculated using  
265 information from only 2 signals, increasing the effects of one noisy trace on  
266 the overall reconstruction. With the addition of more segments in GS 2 and  
267 GS 3, the effects of this on the  $\chi^2$  calculation are reduced.

268 Although the data is all analysed offline, the ultimate goal of this project  
269 would to be capable of utilising Pulse Shape Analysis (PSA) techniques in

Grid Search	Event Processing	Mean Deviation ( $^{\circ}$ / mm)		
		Time (s)	r	$\varphi$
GS 1	0.057	0.0147	1.7919	0.0225
GS 2	0.256	0.0051	1.2515	0.0060
GS 3	0.499	0.0025	1.2045	0.0026

Table 1: Variation in run time per event and position resolution for 3 different combinations of segments when running the grid search algorithm. GS 1 compared the point contact, core and hit segment signals, with GS 2 including the 8 azimuthal segments and GS 3 searching over all segments. For all runs, the normalised RMS noise was set at 0.02, equivalent to a 75 keV  $\gamma$ -ray

270 an online environment, hence the importance of the search time per event.

271 As seen before, there exists a strong relationship between position and  
272 drift time to the point contact. Using this, the drift time can be calculated  
273 from the test pulse, with a cut applied to the database. To calculate the drift  
274 time, the start of the pulse,  $t_0$ , must be accurately determined.

275 Since the point contact pulse remains in the noise for much of its drift,  
276 the  $t_0$  algorithm developed utilises the secondary charge collecting electrode  
277 output. Due to the proximity of the  $\gamma$ -ray interaction to the secondary  
278 collecting electrode, the output pulse exhibits a sharp initial rise enabling  
279 the starting point of the drift to be more accurately determined. This can  
280 be seen in the first interaction in Figure 5. To further exaggerate the initial  
281 rise and also dampen the baseline noise, a cumulative pulse was taken with  
282 each bin comprising of an accumulation of all prior bins. From here, a simple  
283 threshold was set to test that the pulse was starting to rise, in addition to a  
284 check to ensure that the following samples were also rising.

285 Once measured, a drift time cut of  $dt \pm 100$  ns can be applied to the  
286 grid search, reducing the event processing time significantly. When used  
287 in combination with the GS 3 search parameters, the event time reduced  
288 from 0.499 s  $\rightarrow$  0.054 s, with the  $r$ ,  $\varphi$  and  $z$  resolution remaining the same.  
289 A narrower time cut would further reduce the event time, however a more  
290 accurate  $t_0$  calculation would be necessary to ensure the drift times were  
291 calculated correctly.

292 In addition to the drift time cut, a cut on the electron collecting electrode  
293 can be applied to further improve the search time. As seen in Figure 8, for  
294 each segment there exists a small section of the detector wherein a  $\gamma$ -ray  
295 interaction would result in a termination at said electrode. This can be used  
296 to reduce the search space for the grid search algorithm. Combining this  
297 with the drift time cut described above reduces the search time per event  
298 from 0.054 s  $\rightarrow$  0.019 s whilst maintaining the position resolution values seen  
299 in the GS 3 results. For all subsequent studies, the GS 3 search parameters  
300 are used in addition to the drift time and hit segment cuts.

### 301 *3.2. Effects of RMS Noise*

302 One of the main benefits of this detector is the extremely low noise in-  
303 duced on the signals at the point contact. As mentioned earlier, similar point  
304 contact detectors experience peak-to-peak noise values of  $\sim 1$  mV, equating  
305 to a normalised RMS noise of  $\sim 1\%$  at 150 keV. The effects of varying the  
306 noise level from 0  $\rightarrow$  10% at 150 keV have been studied, with the results for  
307 the average deviation presented in Table 2. In addition, a position by posi-  
308 tion scan is illustrated in Figure 9. The percentage of events reconstructed,  
309  $\varepsilon_{recon}$ , to within 1 mm is presented for each study, with the results for 1 and

310 2% RMS noise showing excellent reconstruction capabilities with 100% of  
 311 events reconstructed to within 1 mm of the known interaction position.

Normalised RMS Noise	Mean Deviation ( $^{\circ}$ / mm)			$\varepsilon_{recon}(\%)$ < 1 mm	FWHM (mm)
	r	$\varphi$	z		
0.00	0.0000	0.000	0.0000	100.0	0.00
0.01	0.0004	0.576	0.0004	100.0	0.11
0.02	0.0025	1.205	0.0026	100	0.28
0.05	0.0696	3.535	0.0531	93.0	1.33
0.10	0.3277	7.637	0.2359	40.6	3.52

Table 2: List of mean values from RMS noise simulations, showing average deviation in  $r$ ,  $\varphi$ ,  $z$  for the detector as a whole. The percentage of events reconstructed  $\varepsilon_{recon}$ , to within 1 mm is also shown.

312 The effects of RMS noise are clear, with each increase in noise level result-  
 313 ing in a significant change in the average deviation for all three components.  
 314 By examining each event individually, the 3-dimensional Cartesian position  
 315 variation can also be measured, providing a value more comparable to pub-  
 316 lished results for current state-of-the-art detectors (6; 7). For each event, the  
 317 Cartesian 3-vector between the known position and the reconstructed posi-  
 318 tion was calculated as  $\sqrt{\Delta x^2 + \Delta y^2 + \Delta z^2}$ , where  $\Delta x$ ,  $\Delta y$  and  $\Delta z$  represent  
 319 the deviation in each of the respective dimensions. The FWHM was then  
 320 calculated as

$$FWHM = 2.35\sigma = 2.35\sqrt{\frac{\sum_N \Delta_{x,y,z}^2}{N}} \quad (3)$$

321 where  $\Delta_{x,y,z}$  is the Cartesian 3-vector. The position resolution was calculated

322 as 0.105, 0.281, 1.332 and 3.515 mm for 1, 2, 5 and 10 % RMS noise respec-  
323 tively. This is substantially better than the current  $\sim 4.5 - 5$  mm attainable  
324 by AGATA at 1.3 MeV (6) and GRETINA at 2 MeV (7).

325 Figure 9 shows the distribution of the erroneous reconstructions follows  
326 the segmentation scheme seen in Figure 8, with the increase in RMS noise  
327 showing this effect more clearly. The addition of a segment cut results in a  
328 larger error near the centre of segments, with the errors on the boundaries  
329 significantly reduced. This plot also shows the much greater resolution in  $z$   
330 than  $r$ , with the cut on drift time providing a clear  $z$  position for the front  
331 end of the detector. The  $r$  resolution arises in part due to the cut on segment,  
332 with the core segment showing the worst resolution in  $r$  as a consequence of  
333 its size. The resolution in  $\varphi$  is poorest near  $r = 0$  mm, something that is  
334 likely caused by the much smaller deviation in drift time as a function of  $\varphi$   
335 at small drift times, hence more similar charge pulses in these regions. It  
336 is also worth noting that larger errors in  $\varphi$  in these regions have less of an  
337 effect on the 3-dimensional deviation due to them being closer to the central  
338 axis. This is related to the fact that the distance,  $d$ , between two positions  
339 separated by angle,  $\varphi$ , at a constant radius,  $R$ , is given by  $d = 2R\sin(\frac{\varphi}{2})$ .

340 When reconstructing  $\gamma$ -ray tracks within a detector, the majority of in-  
341 teractions will be low energy Compton scatters in the 100 - 500 keV range,  
342 which when reconstructed sum to equal the initial  $\gamma$ -ray energy. This study  
343 shows that even at low energy, SIGMA will be capable of providing excep-  
344 tional position resolution. For higher  $\gamma$ -ray energies, the relative contribution  
345 of the noise is reduced and hence these values will be improved upon.

346 One thing to consider when performing a realistic simulation is the fact

347 that electron collecting electrodes, segments 1-19, are much larger in size  
348 than the point contact. This increased size results in a higher capacitance  
349 and hence increased series noise. To account for this, a realistic peak-to-peak  
350 noise, ranging from 5mV  $\rightarrow$  15 mV has been added to each segment according  
351 to their relative sizes. When applying this to the 1% RMS noise simulation  
352 presented in Table 2, the FWHM for the position resolution decreases from  
353 0.11  $\rightarrow$  0.41 mm.

### 354 *3.3. Effects of Pulse Alignment*

355 One experimental challenge to PSA lies in the ability to accurately de-  
356 termine the start time of the pulse,  $t_0$ . As seen earlier in Figure 7, the drift  
357 time to the point contact contains information regarding interaction position.  
358 However, due to the compact nature of the point contact weighting poten-  
359 tial, the pulses remain near the baseline for much of that drift as shown in  
360 Figure 4. This increases the difficulty in determining  $t_0$ .

361 To study the effects of incorrectly identifying  $t_0$ , a random shift was  
362 assigned to each test pulse within the range -n...n, where n is the maximum  
363 number of samples to be shifted. The results for the mean response to an  
364 alignment shift of 0  $\rightarrow$  4 samples, equating to 0  $\rightarrow$  40 ns, is presented in  
365 Table 3, with Figure 10 showing the variation in the reconstructed position  
366 relative to the true position at  $\varphi = 0^\circ$  for each position in the detector on a  
367  $1 \times 1$  mm grid. To isolate the effects of  $\Delta t_0$ , the RMS noise was set to 0 for  
368 this study.

369 Again, the results for  $\Delta t_0 = 0$  show perfect reconstruction, with a  $\Delta t_0$   
370 of  $\pm 10$  ns having a significant effect on the reconstruction efficiency with  
371 57.9% of the  $\gamma$ -ray interactions reconstructed to within 1 mm of the known

$\Delta t_0$ (ns)	Mean Deviation ( $^\circ$ / mm)			$\varepsilon_{recon}(\%)$	FWHM (mm)
	$r$	$\varphi$	$z$		
0	0.000	0.000	0.000	100.0	0.00
10	0.327	5.597	0.253	57.9	3.10
20	0.698	7.744	0.573	40.2	4.85
30	0.968	9.228	0.859	30.7	6.11
40	1.208	10.138	1.132	24.9	7.18

Table 3: List of mean deviation as a function of  $\Delta t_0$ , showing average deviation in  $r$ ,  $\varphi$  and  $z$  for the detector as a whole. The percentage of events reconstructed  $\varepsilon_{recon}$ , to within 1 mm is also shown.

372 interaction position. The 3-dimensional FWHM is also reduced to 3.10 mm  
373 for  $\Delta t_0 = 10$  ns, demonstrating the importance of correctly aligning experi-  
374 mental pulses with those in the database. As can be seen, a single channel  
375 misalignment in a 100 MHz digitiser output signal has the same effect as  
376 increasing the RMS noise to 10 %.

377 The importance of this effect is clear to see, with the variation in  $r$ ,  $\varphi$   
378 and  $z$  more than doubling from  $\Delta t_0 = 10 \rightarrow 40$  ns. The percentage of events  
379 reconstructed to within 1 mm more than halved from  $\Delta t_0 = 10 \rightarrow 40$  ns. The  
380 3-dimensional position resolution is also significantly reduced at  $\Delta t_0 = 40$  ns  
381 with FWHM = 7.18 mm.

382 To combat this, additional searches can be added to the grid search algo-  
383 rithm, whereby the pulses in the database are compared with the test pulse  
384 using multiple different alignments. Applying this methodology to the worst  
385 case studied,  $\Delta t_0 = 40$  ns, with the search space expanded to cover shifts of  
386 up to  $\pm 2$  bins, the 3-dimensional position resolution improved from 7.18  $\rightarrow$

387 5.04 mm.

### 388 *3.4. Expected Position Resolution*

389 SIGMA will have a large variety of spectroscopic applications both as a  
390 standalone detector and as part of an array in conjunction with ancillary sys-  
391 tems. The performance of SIGMA as a tracking and imaging system will vary  
392 in each case with the increased information available from ancillary detec-  
393 tors aiding in SIGMA's position reconstruction capabilities. Two scenarios  
394 are presented here; SIGMA as a standalone system and SIGMA in conjunc-  
395 tion with an implantation detector as would be the case at the DESPEC  
396 experiment at FAIR. The advantages of using an implantation detector lie  
397 in the ability to perform temporal correlations between implantations in the  
398 ancillary and interactions in SIGMA. This should enable proper alignment  
399 of pulses to within a single digitiser sample, i.e.  $<10$  ns.

400 For a more thorough understanding of the performance of SIGMA in  
401 real situations, the effects described in Section 3 must be collated using  
402 realistic values for each scenario. To create the realistic test pulses, a peak-  
403 to-peak noise of 1 mV was added to the point contact signal of each pulse. In  
404 addition, peak-to-peak noise ranging from 5  $\rightarrow$  15 mV was added to segments  
405 1-19. Simulations are presented for initial  $\gamma$ -ray energies of 500 keV and 1  
406 MeV. In addition to the series noise, a pulse alignment error was included  
407 to represent the expected errors for each of the 2 scenarios studied. For  
408 standalone SIGMA, a pulse alignment error of  $\pm 30$  ns was used with a value  
409 of  $\pm 10$  ns used for the simulations with an ancillary detector. In all studies,  
410 the pulses were processed through the GS 3 algorithm with cuts placed on  
411 both the drift time and hit segment with the search space extended to cover

412  $t_0 \pm 2$  s.

413 The results are presented in Table 4 showing the mean deviation in  $r$ ,  $\varphi$   
 414 and  $z$ , along with the FWHM of the Cartesian 3-vector between the known  
 415 and reconstructed positions. As a standalone detector, SIGMA will be capa-  
 416 ble of providing an exceptional position resolution of 4.54 mm at 500 keV. and  
 417 4.37 mm at 1 MeV. These values are significantly improved when SIGMA is  
 418 paired with an ancillary detector capable of improving the  $t_0$  determination  
 419 of the pulses. As seen in Table 4, the FWHM for SIGMA with an ancillary  
 420 detector is 0.65 mm at 500 keV and 0.33 mm at 1 MeV. These values would  
 421 represent an improvement over current large volume germanium detectors.  
 422 One note regarding these results is the fact that the simulations do not ac-  
 423 count for the finite size of the electron charge cloud and the resulting charge  
 424 sharing effects that occur near segment boundaries. These effects will be  
 425 studied in more detail during the experimental phase of this project.

	$E_\gamma$ (keV)	Mean Deviation			FWHM
		$r$ (mm)	$\varphi$ ( $^\circ$ )	$z$ (mm)	(mm)
Standalone	500	0.570	7.612	0.451	4.54
	1000	0.535	7.124	0.424	4.37
w Ancillary	500	0.049	1.347	0.036	0.64
	1000	0.006	0.533	0.006	0.33

Table 4: List of mean deviation for two configurations of SIGMA at initial  $\gamma$ -ray energies of 500 keV and 1 MeV showing the average deviation in  $r$ ,  $\varphi$  and  $z$  for the detector as a whole. Also presented is the FWHM for the Cartesian 3-vector between the known position and the reconstructed position.

#### 426 **4. Conclusion**

427 The SIGMA detector should be capable of providing unrivalled position  
428 and energy resolution, with its unique design enabling major advancements  
429 over current state-of-the art large volume HPGe detectors used in the track-  
430 ing arrays AGATA and GRETA. A limiting theoretical estimate suggests a  
431 3-dimensional position resolution ranging from 0.41 mm at 150 keV to 0.33  
432 mm at 1 MeV. Performance such as this will aid in drastically improving the  
433 tracking and imaging capabilities of large volume HPGe detectors. With a  
434 more accurate and consistent determination of  $t_0$ , tighter cuts on the drift  
435 time can be applied, decreasing the time taken to scan a single event in  
436 addition to providing much tighter constraints on the interaction position.

#### 437 **5. Acknowledgements**

438 This research was supported by the United Kingdom Science and Technol-  
439 ogy Facilities Council (STFC UK) grant ST/M003582/1 and the U.S Depart-  
440 ment of Energy, Office of Science, Office of Nuclear Physics, under contract  
441 number DE-AC05-00OR22725. The authors would also like to acknowledge  
442 the contributions of Karin Lagergren, Ren Cooper and Heather Crawford.

443 [1] R. Cooper et al., A novel HPGe detector for gamma-ray tracking and  
444 imaging, *Nuc. Instr. Meth. A* 665 (2011) 25–32.

445 [2] M. Salathe et al., Energy reconstruction of an n-type segmented inverted  
446 coaxial point-contact HPGe detector, *Nucl. Instr. Meth. A* 868 (2017)  
447 19–26.

- 448 [3] B. Rubio, Decay Spectroscopy (DeSpec) at the New FAIR-NuSTAR  
449 Facility, *Int. Jour. Mod. Phys. E* 15 (2006) 1979–1988.
- 450 [4] L. Harkness-Brennan et al., An Experimental Characterisation of a  
451 Broad Energy Germanium Detector, *Nucl. Instr. Meth. A* 760 (2014)  
452 28–39.
- 453 [5] K. Vetter et al., Three-dimensional Position Sensitivity in Two-  
454 dimensionally Segmented HPGe Detectors, *Nucl. Instr. Meth. A* 452  
455 (2000) 223–238.
- 456 [6] F. Recchia et al., Position resolution of the prototype AGATA triple-  
457 cluster detector from an in-beam experiment, *Nucl. Instr. Meth. A* 604  
458 (2009) 555–562.
- 459 [7] M. Descovich et al., In-beam measurement of the position resolution of  
460 a highly segmented coaxial germanium detector, *Nucl. Instr. Meth. A*  
461 553 (2005) 535–542.
- 462 [8] D. Radford, et al., FieldGen/SigGen software, available by svn at [http:  
463 //radware.phy.ornl.gov/MJ/ic\\_siggen/](http://radware.phy.ornl.gov/MJ/ic_siggen/).
- 464 [9] W. Shockley, Currents to Conductors Induced by a Moving Point  
465 Charge, *J. Appl. Phys* 9 (1938) 635.
- 466 [10] S. Ramo, Currents Induced by Electron Motion, *Proceedings of the I.R.E*  
467 September (1939) 584.
- 468 [11] Z. He., Review of the Shockley-Ramo theorem and its application in

- 469 semiconductor gamma-ray detectors, Nucl. Instr. Meth. A 463 (2000)  
470 250–267.
- 471 [12] L. Mihailescu et al., The influence of anisotropic electron drift velocity  
472 on the signal shapes of closed-end HPGe detectors, Nucl. Instr. Meth.  
473 A 447 (2000) 350–360.
- 474 [13] S. Akkoyun, et al., Nucl. Instr. Meth. A 668 (2012) 26.
- 475 [14] G. Schmid et al., A  $\gamma$ -ray tracking algorithm for the GRETA spectrom-  
476 eter, Nucl. Instr. Meth. A 430 (1999) 69–83.
- 477 [15] W. Jung, Op Amp Applications Handbook, Newnes, 2002.

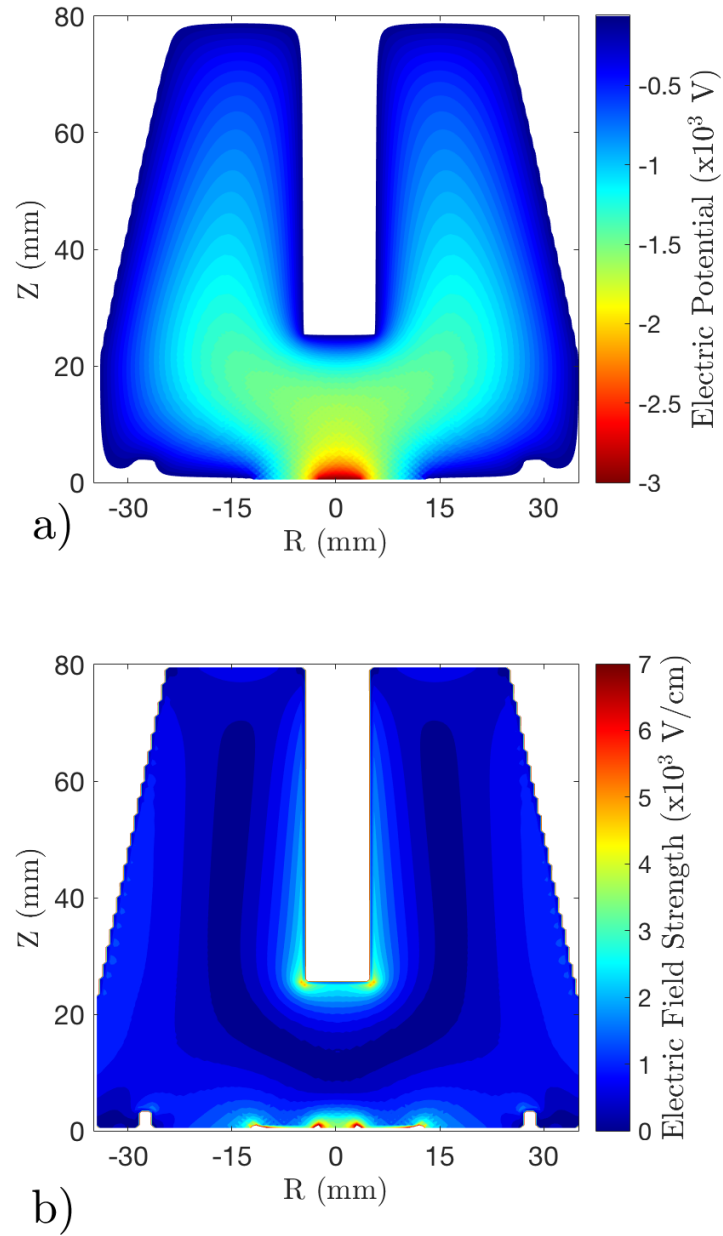


Figure 3: (a) The simulated electric potential and (b) the simulated electric field strength of the SIGMA detector showing the short range of the electric potential and also the very weak fields present in the bulk of the crystal (colour online).

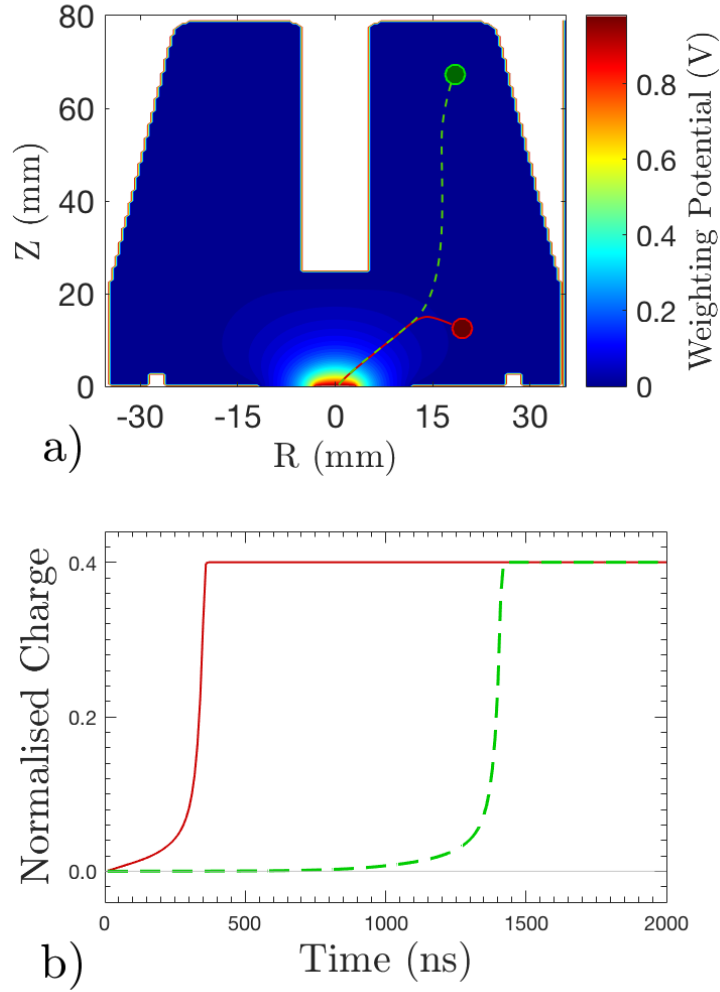


Figure 4: (a) The weighting potential for the point contact and (b) two example point contact charge pulses resulting from  $\gamma$ -ray interaction occurring in different locations within the detector. The red (solid) and green (dashed) circles in (a) represent the positions of the two  $\gamma$ -ray interactions that produce the signals shown in (b) with the charge drift paths overlaid. There exists a clear temporal variation in the signals; a feature that enables multiple interactions to be more easily identified (colour online).

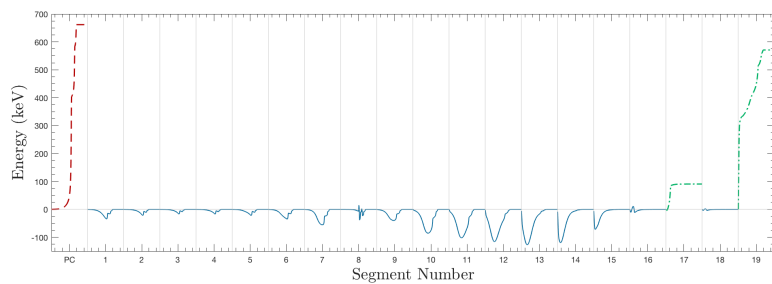


Figure 5: Example pulses from a multi site event interacting in the SIGMA detector. The terminating electrode of the holes and electrons are highlighted in red (dashed) and green (dot-dashed) respectively, with all image charges shown in blue (solid) (colour online).

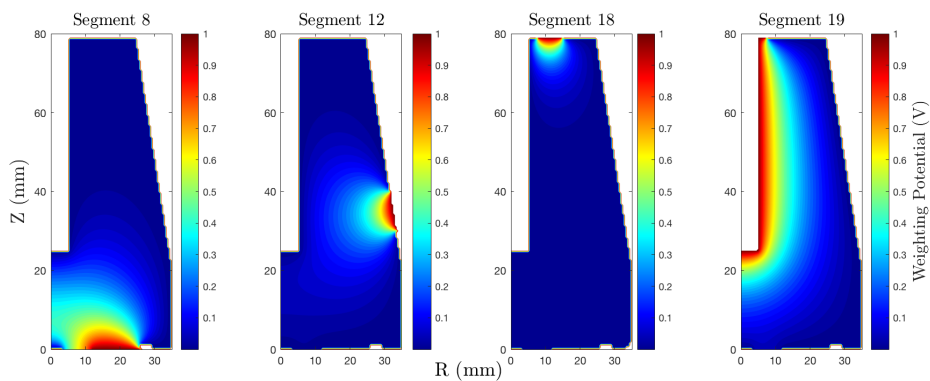


Figure 6: Simulated weighting potentials through the central axis for four segments in the SIGMA detector. Only 1 potential is calculated for the azimuthal segments with the same potential used for each (colour online).

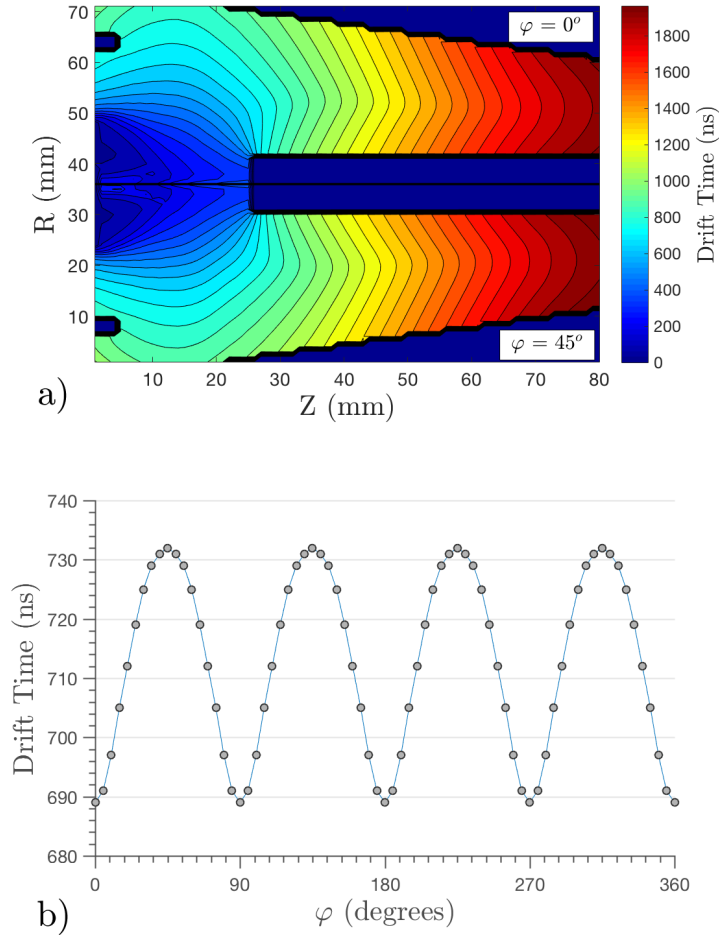


Figure 7: (a) Drift time distribution as a function of  $\gamma$ -ray interaction position within the detector. Overlaid are 50 ns isochrones. The top half of the figure shows results for  $\varphi = 0^\circ$ , with the lower half showing  $\varphi = 45^\circ$ , with a slight variation seen in the drift patterns between the two as a result of the change in crystallographic axis with varying  $\varphi$ . (b) Variation in drift time as a function of  $\varphi$  for a  $\gamma$ -ray interaction at  $(r, z) = (20, 20)$  mm, showing the  $\sim 6\%$  peak-to-peak change from  $0^\circ \rightarrow 45^\circ$  (colour online).

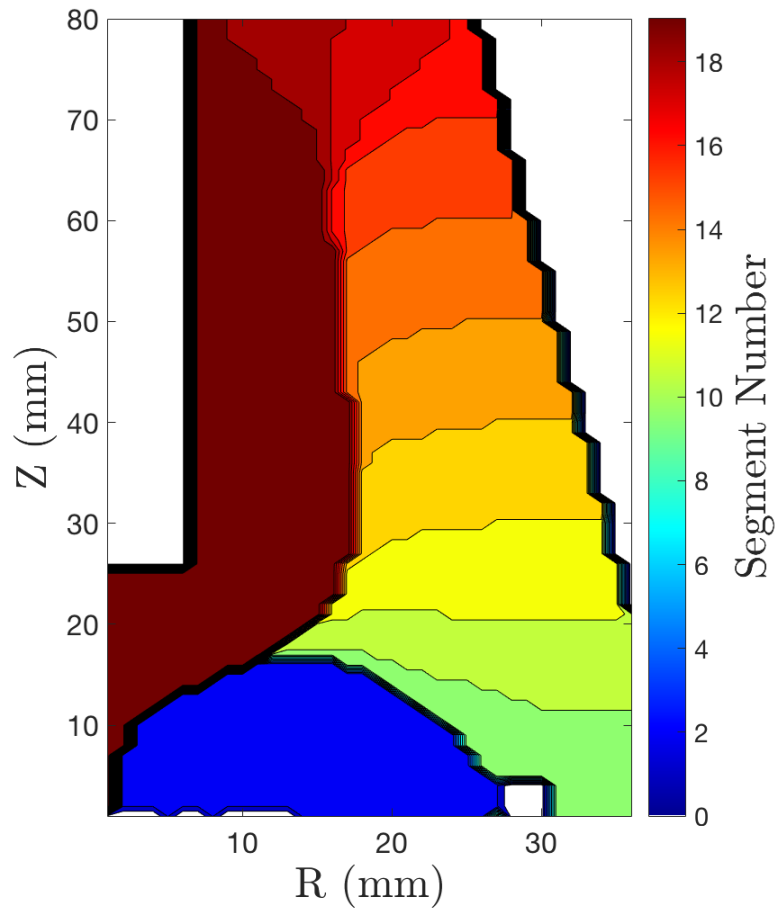


Figure 8: Illustration of the secondary collecting electrode as a function of  $\gamma$ -ray interaction position within the detector (colour online).

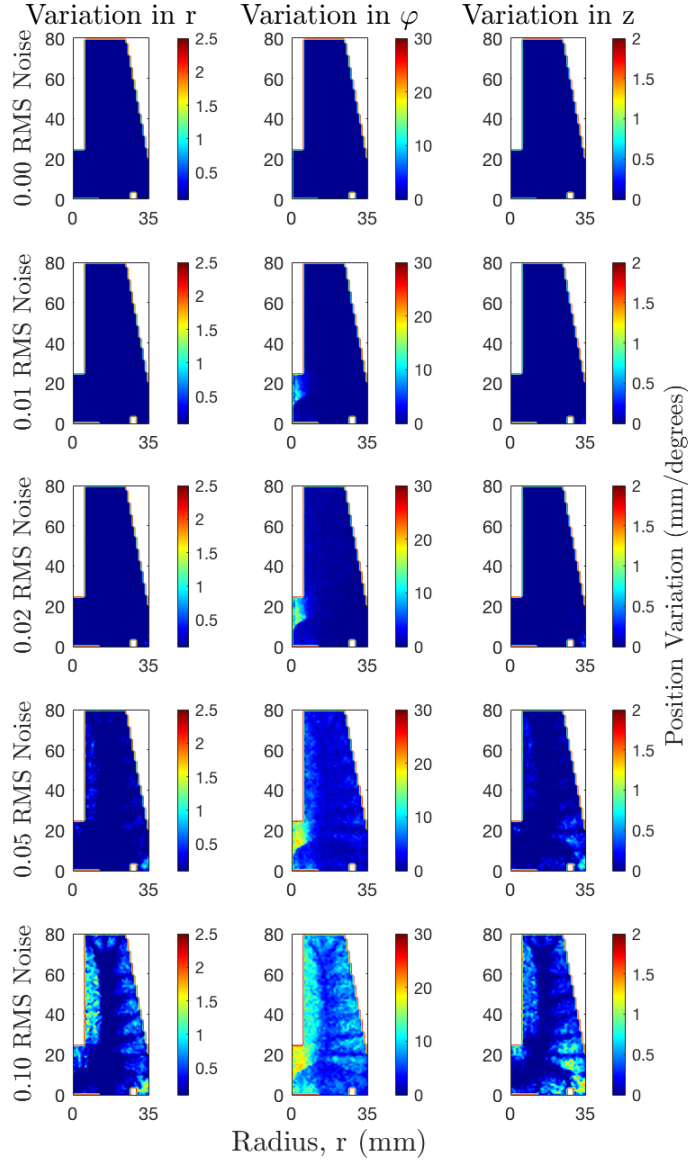


Figure 9: Deviation of reconstructed position from true position as a function of RMS noise, using the GS 3 algorithm in addition to cuts placed on the drift time ( $\pm 100$  ns) and hit segment. Deviations for  $r$ ,  $\varphi$  and  $z$  are shown in the left, middle and right panels respectively in units of mm and  $^\circ$  (colour online).

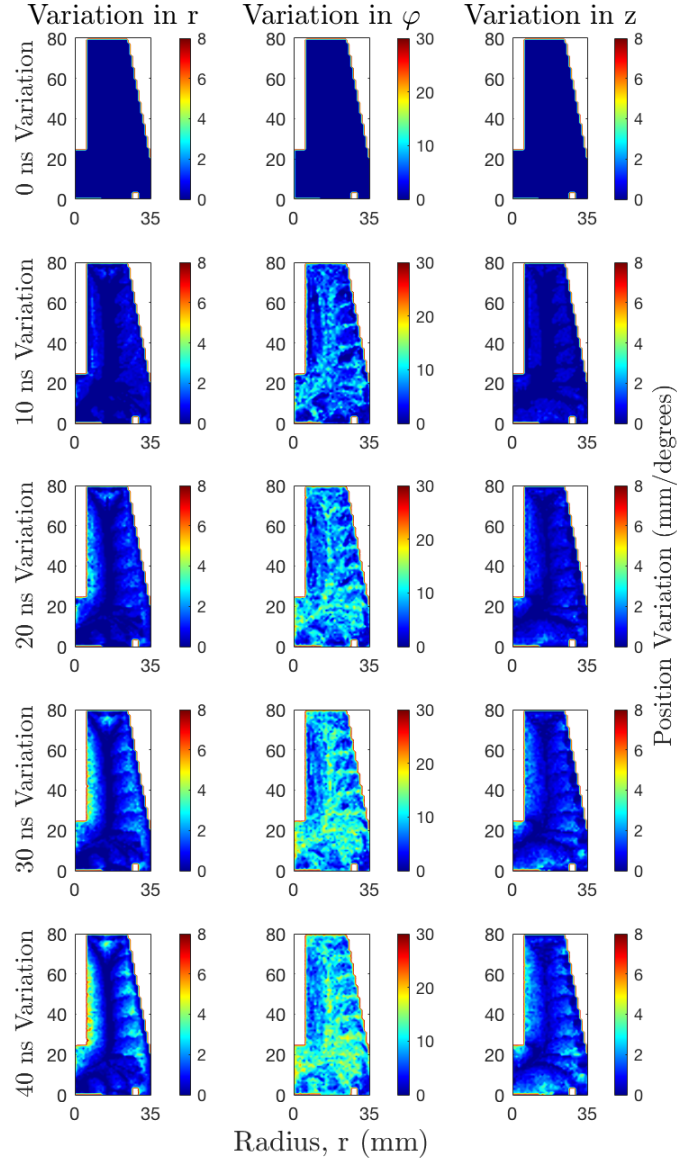


Figure 10: Deviation of reconstructed position from true position as a function of pulse alignment error, using the GS 3 algorithm in addition to cuts placed on the drift time ( $\pm 100$  ns) and hit segment. Deviations for  $r$ ,  $\varphi$  and  $z$  are shown in the left, middle and right panels respectively in units of mm and  $^\circ$  (colour online).

Figure 1

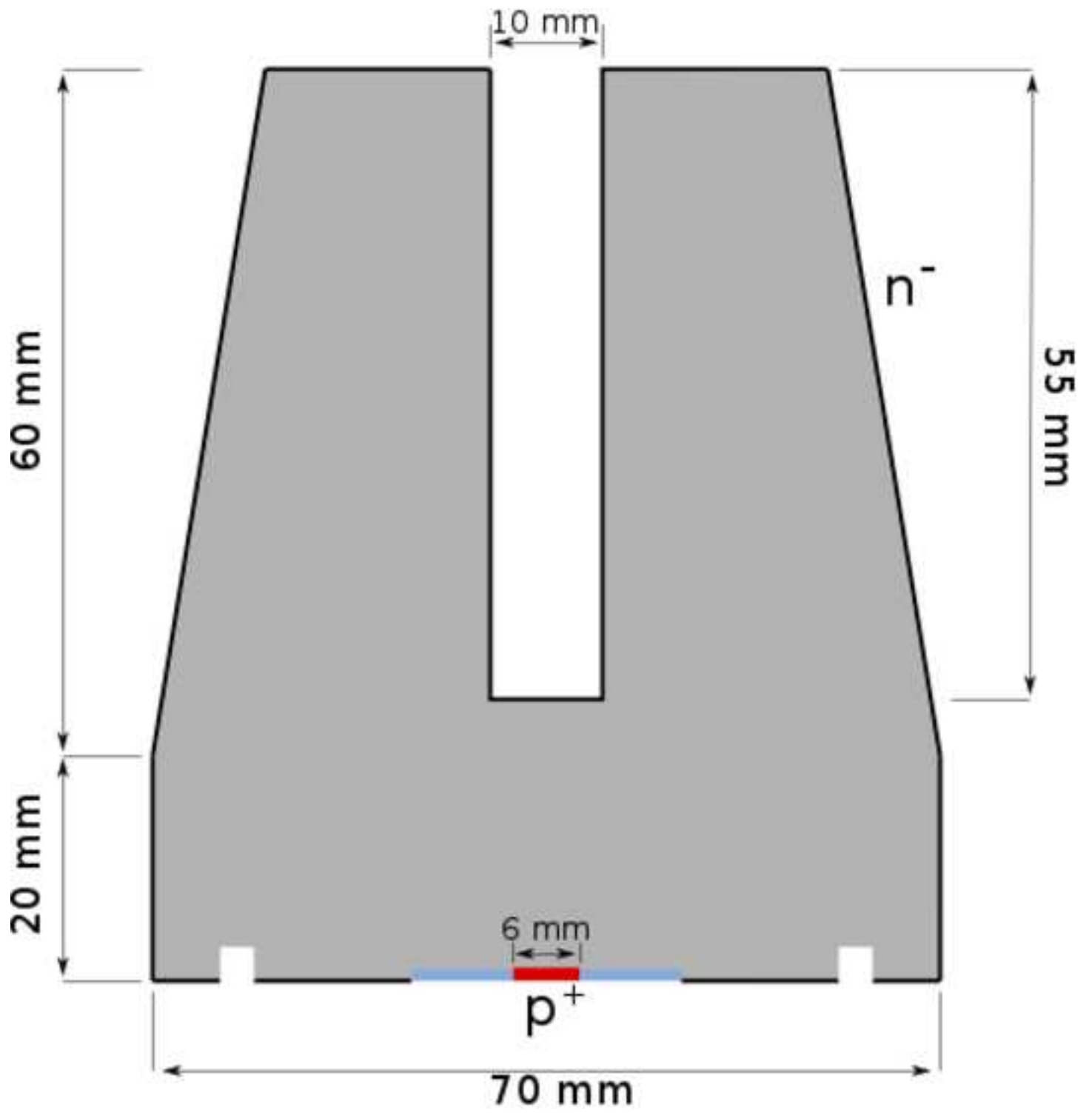


Figure2

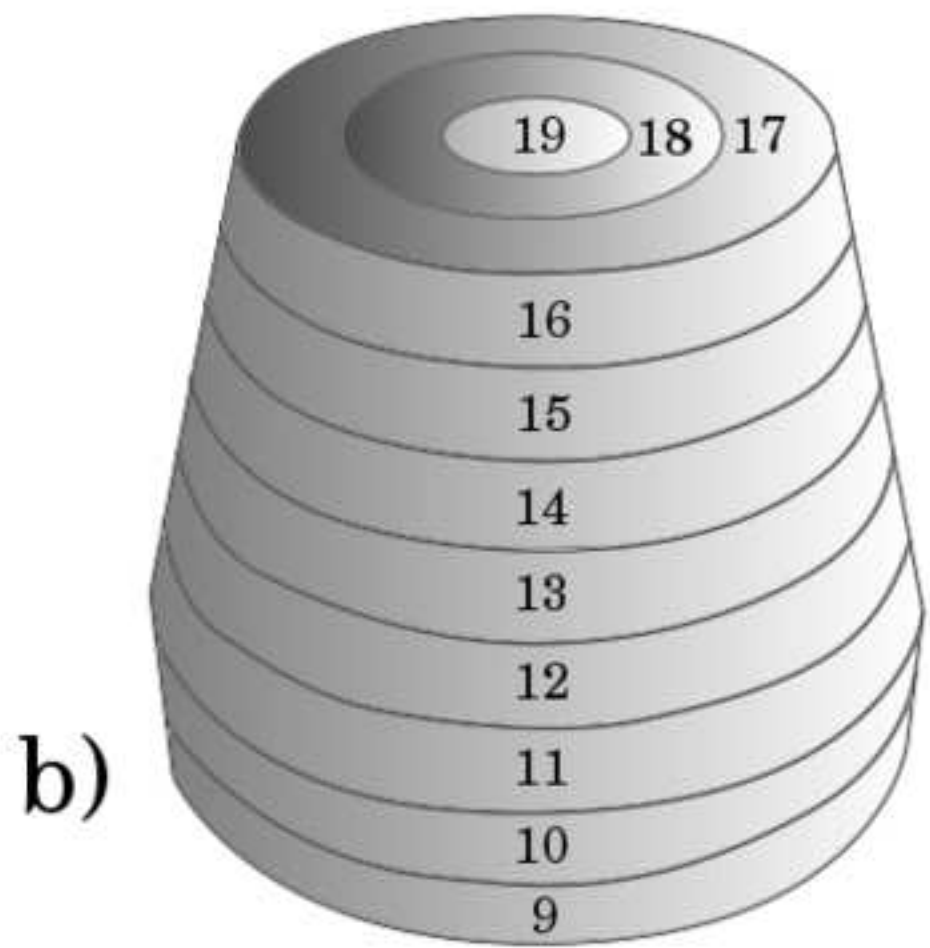
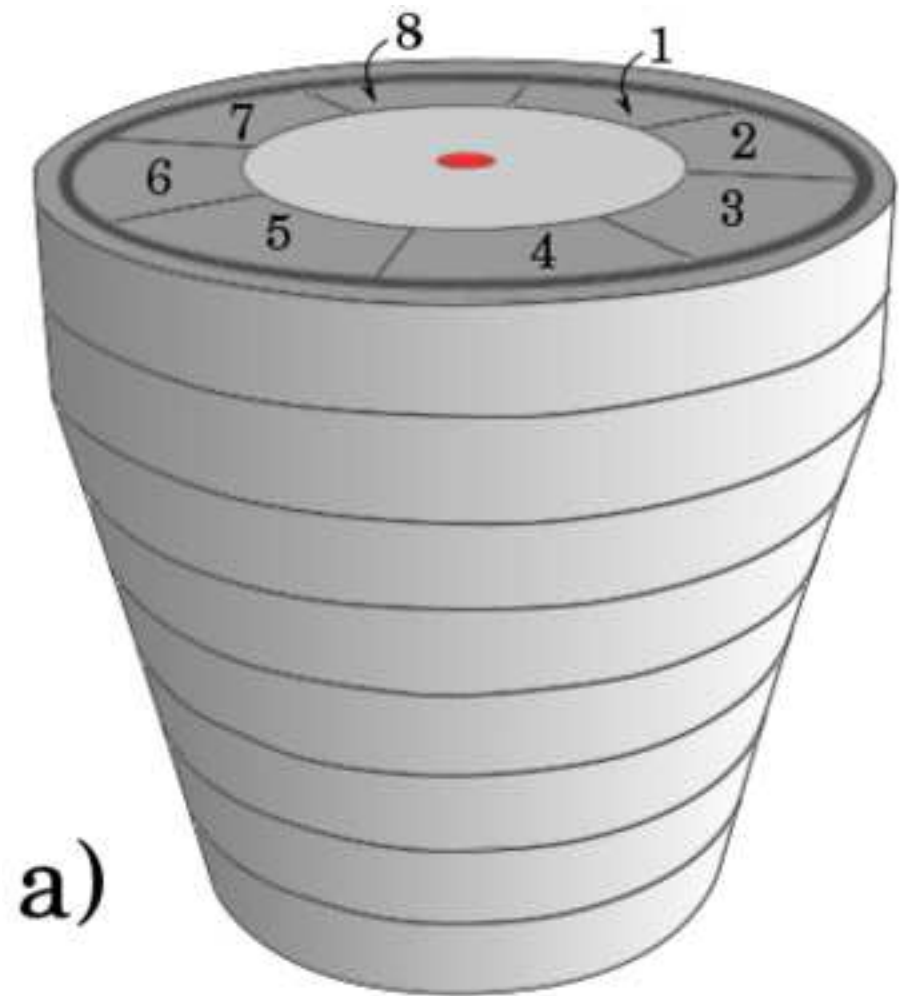


Figure3

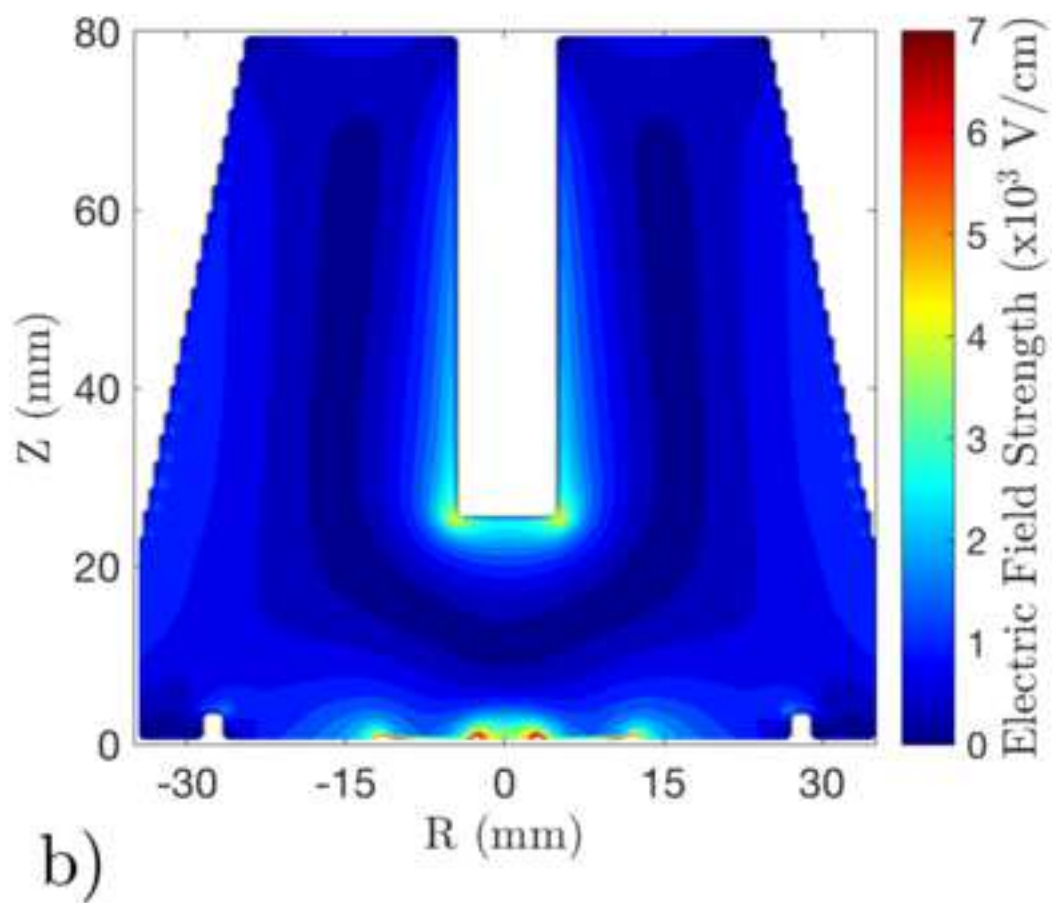
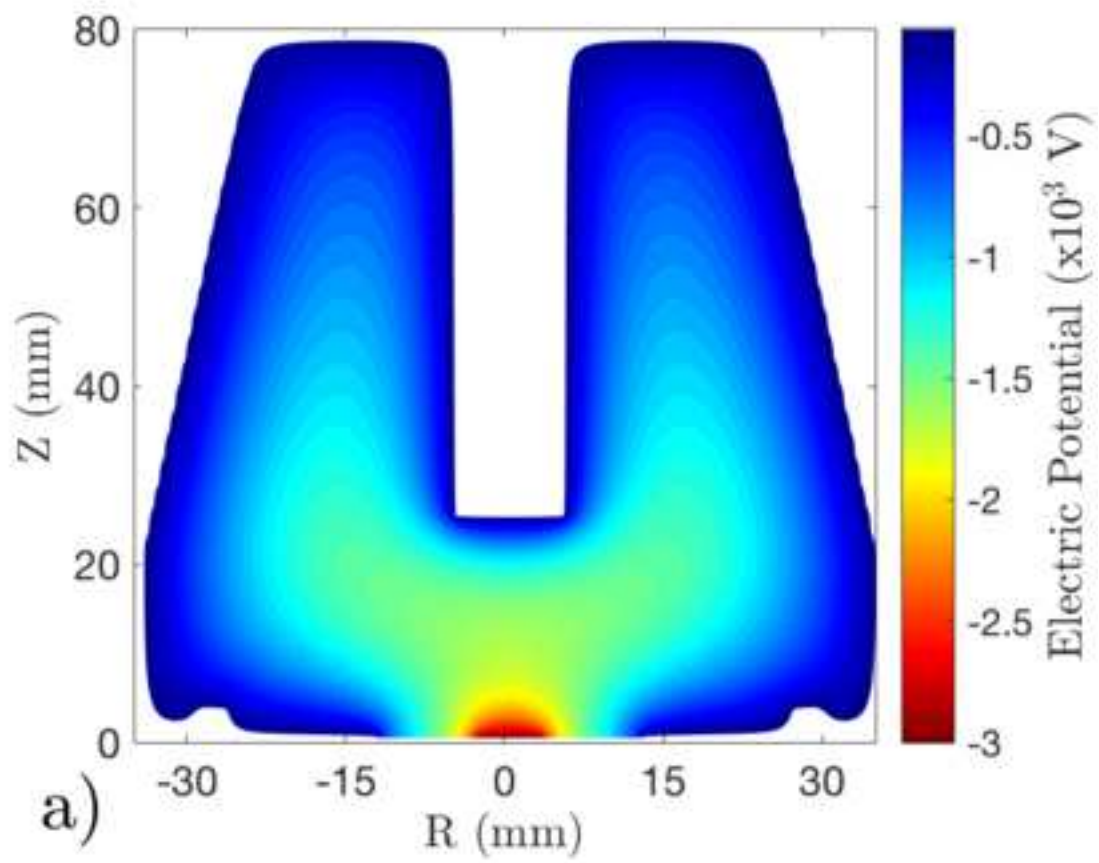


Figure4

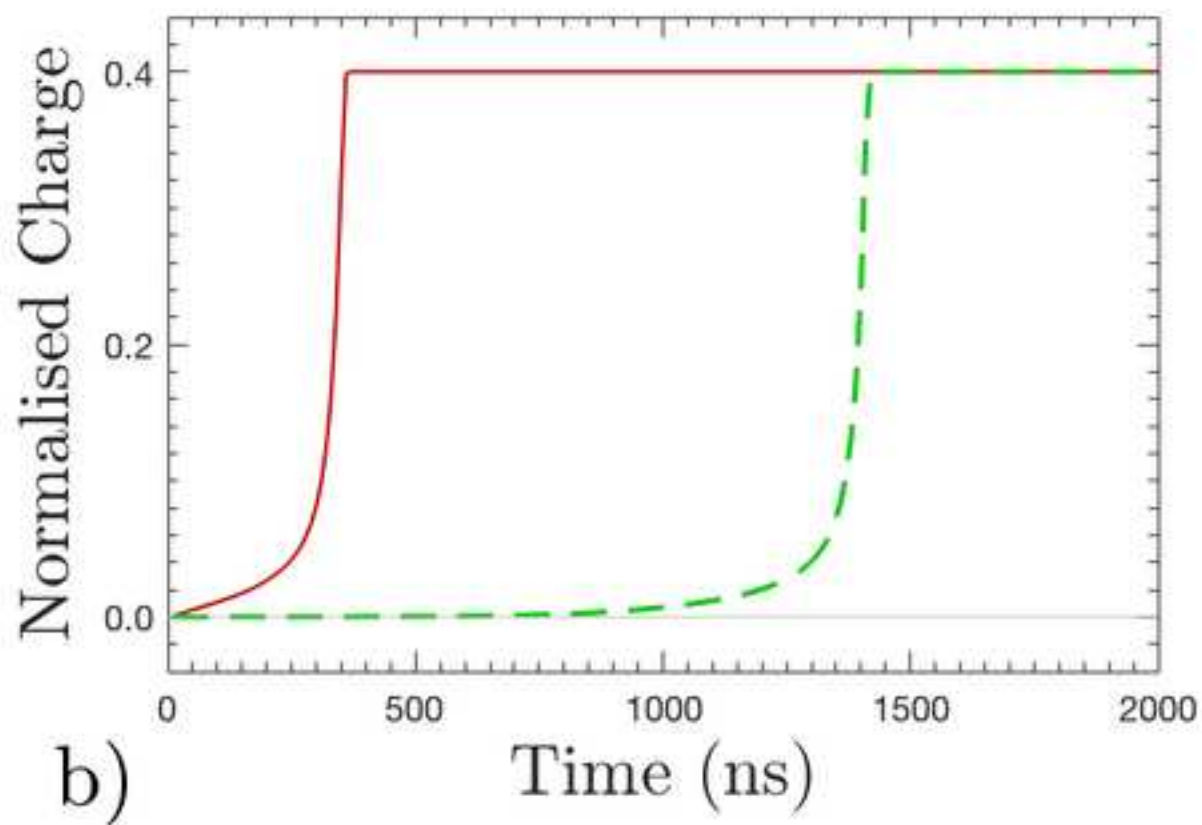
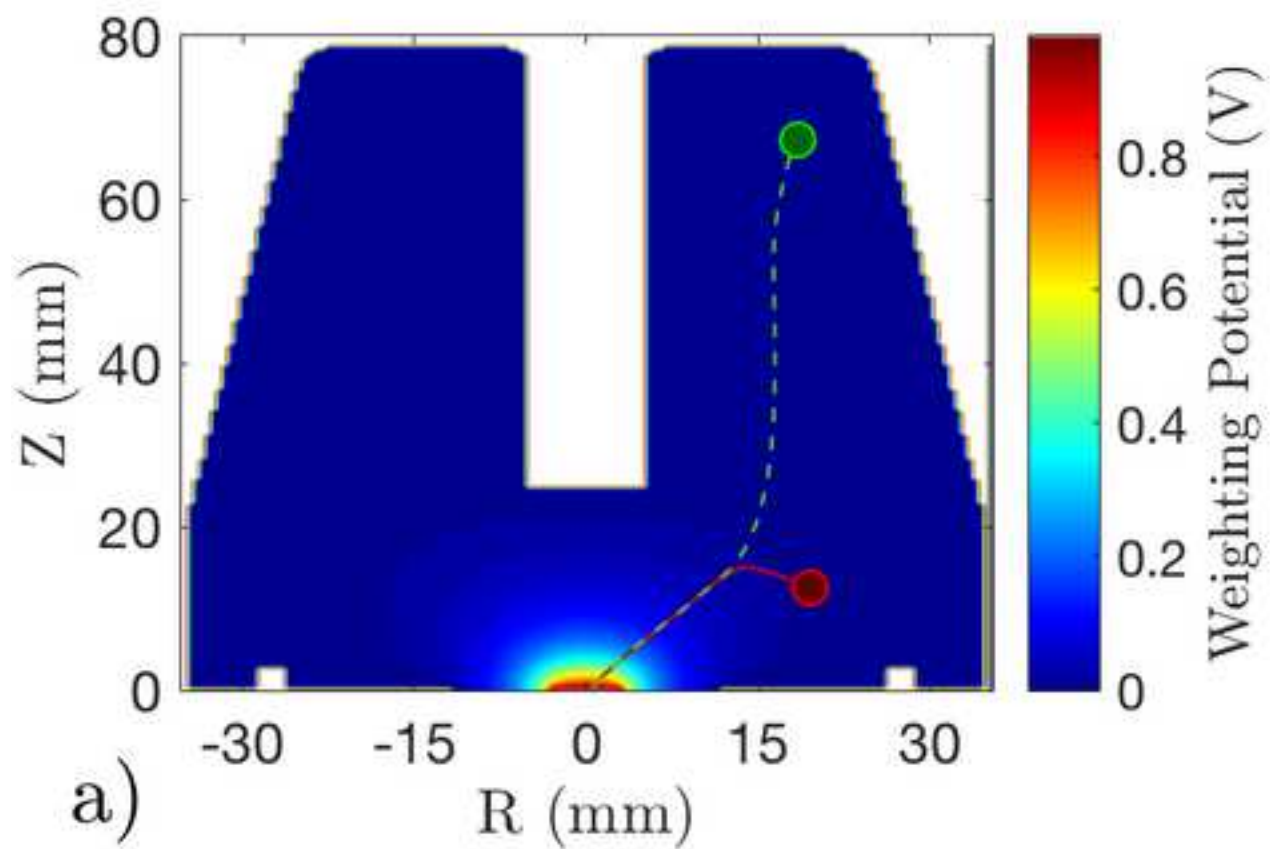


Figure 5

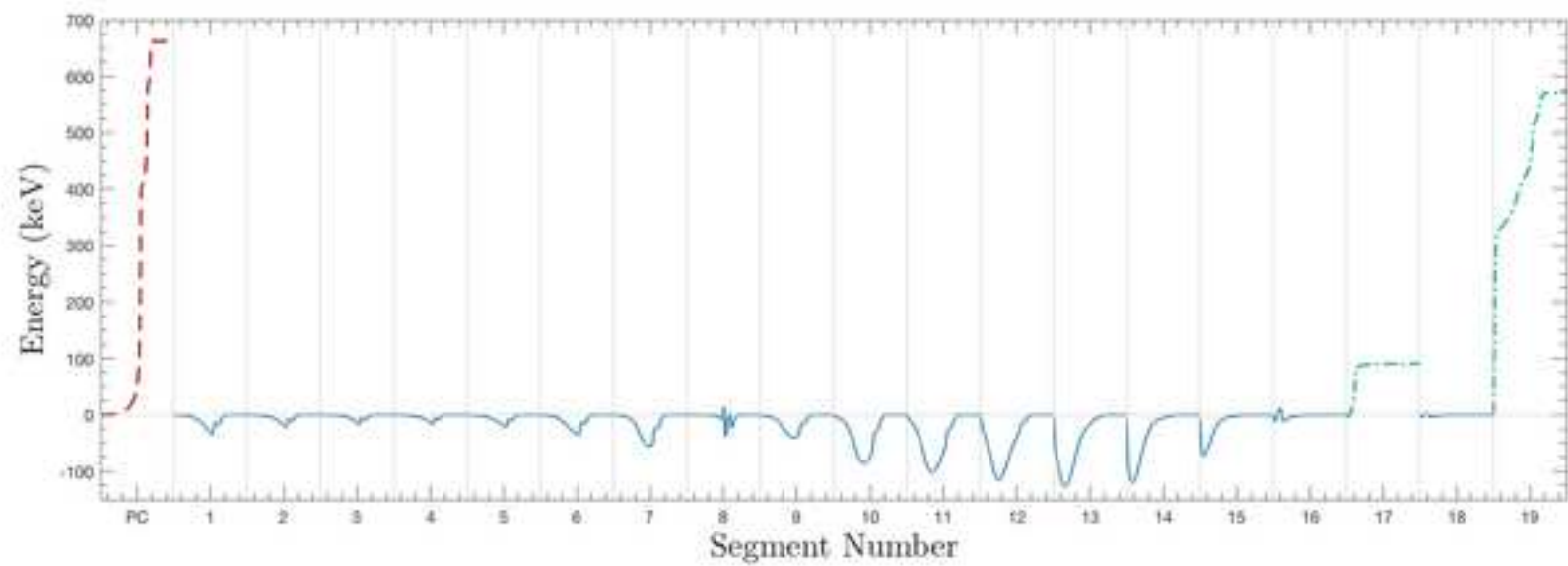


Figure6

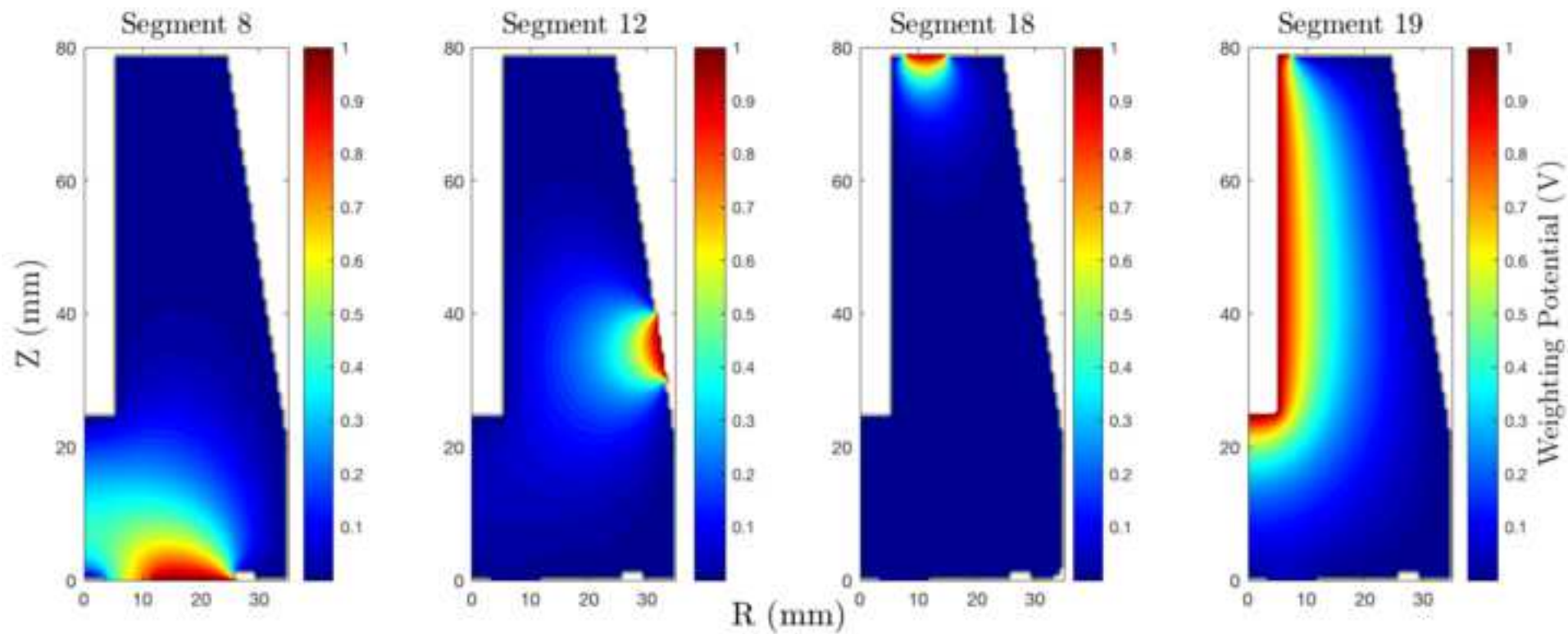


Figure 7

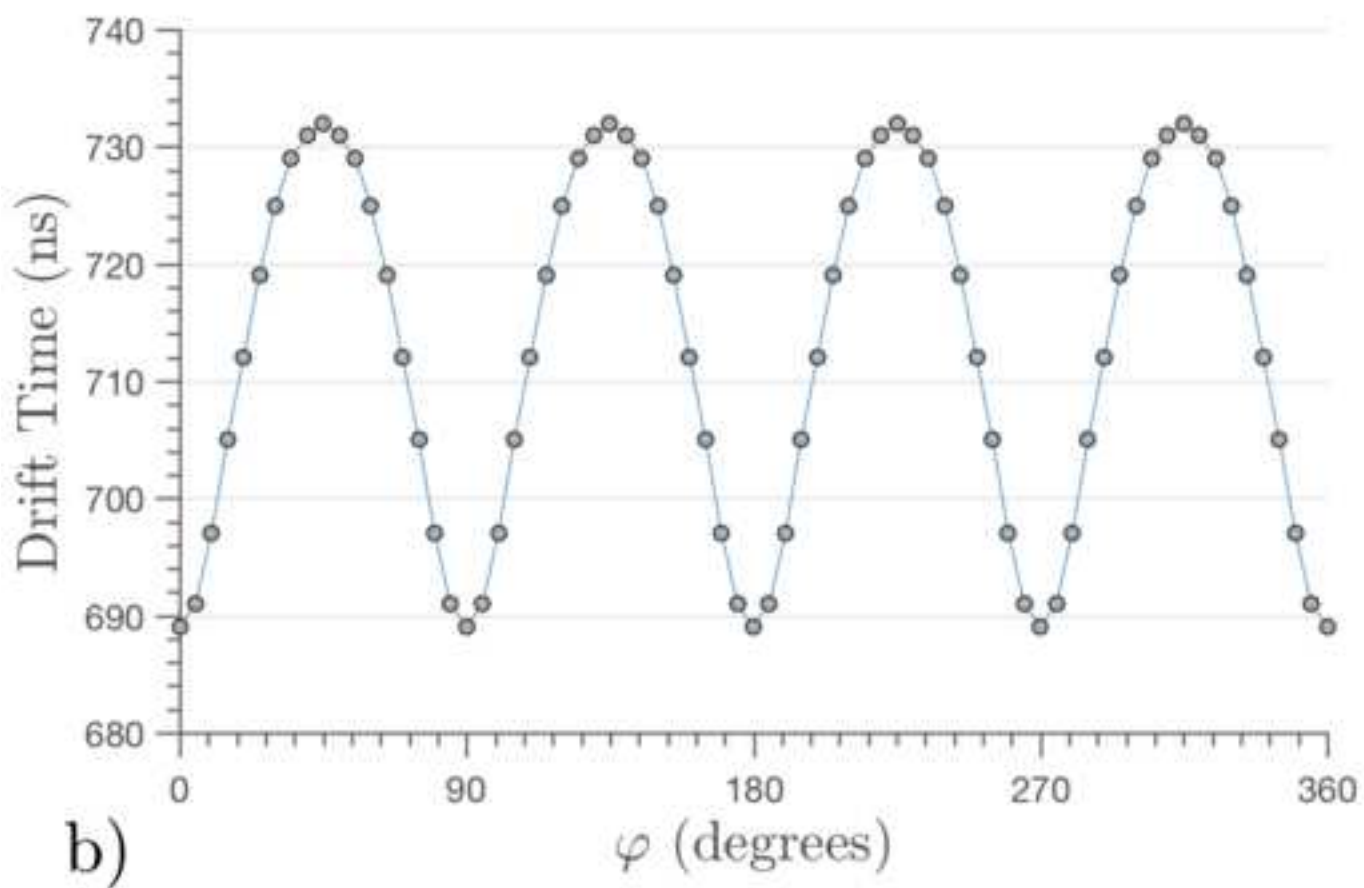
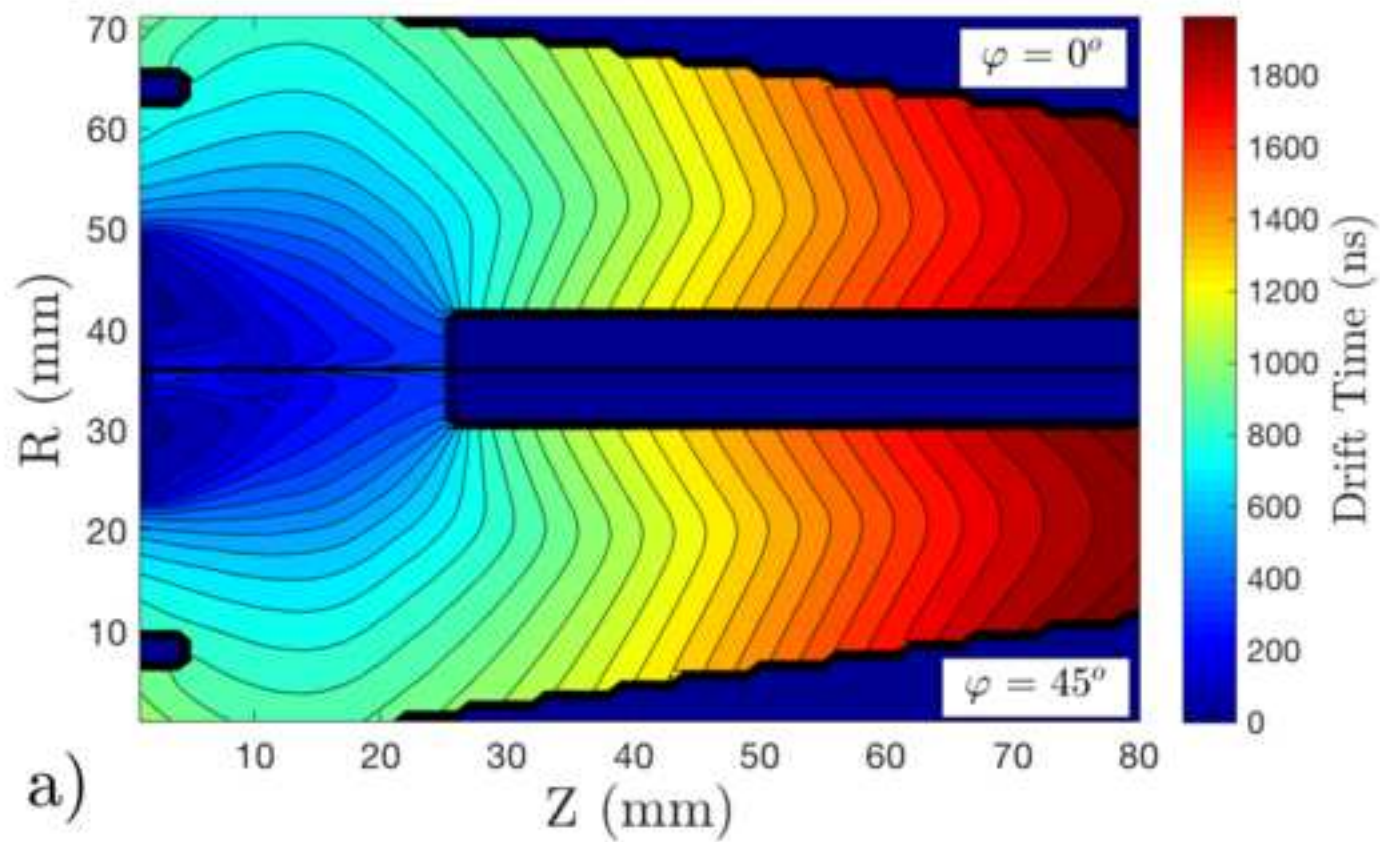


Figure8

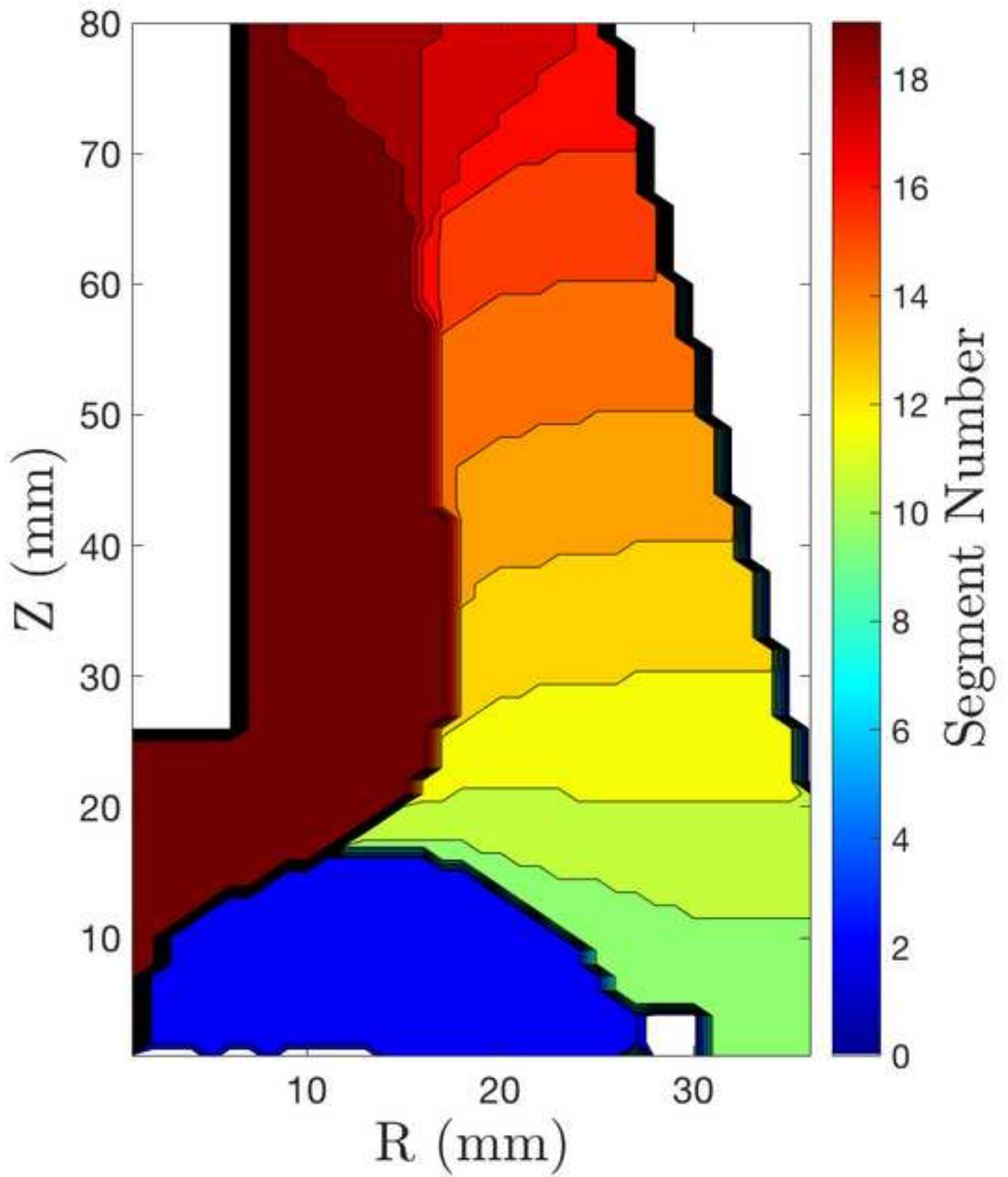


Figure9

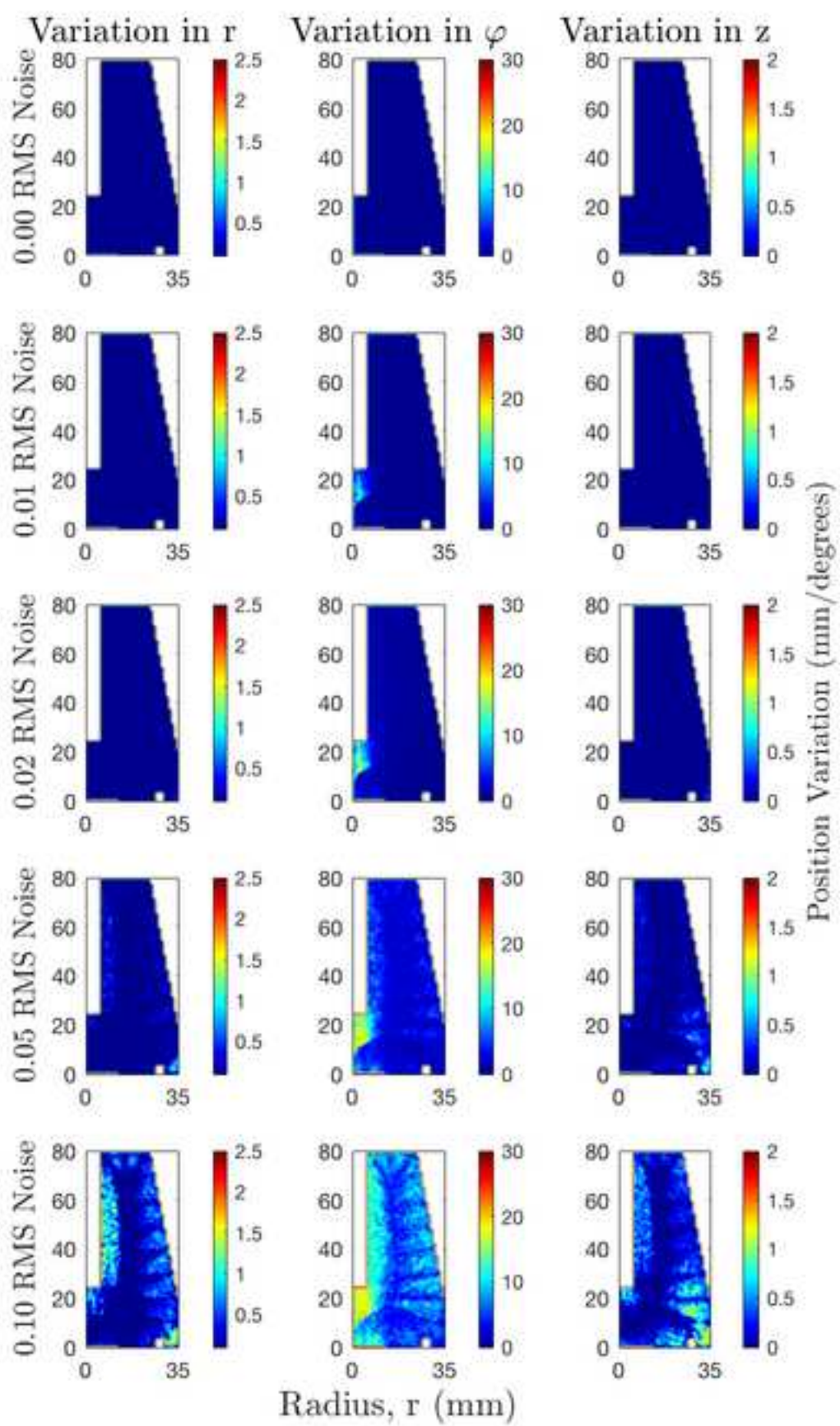
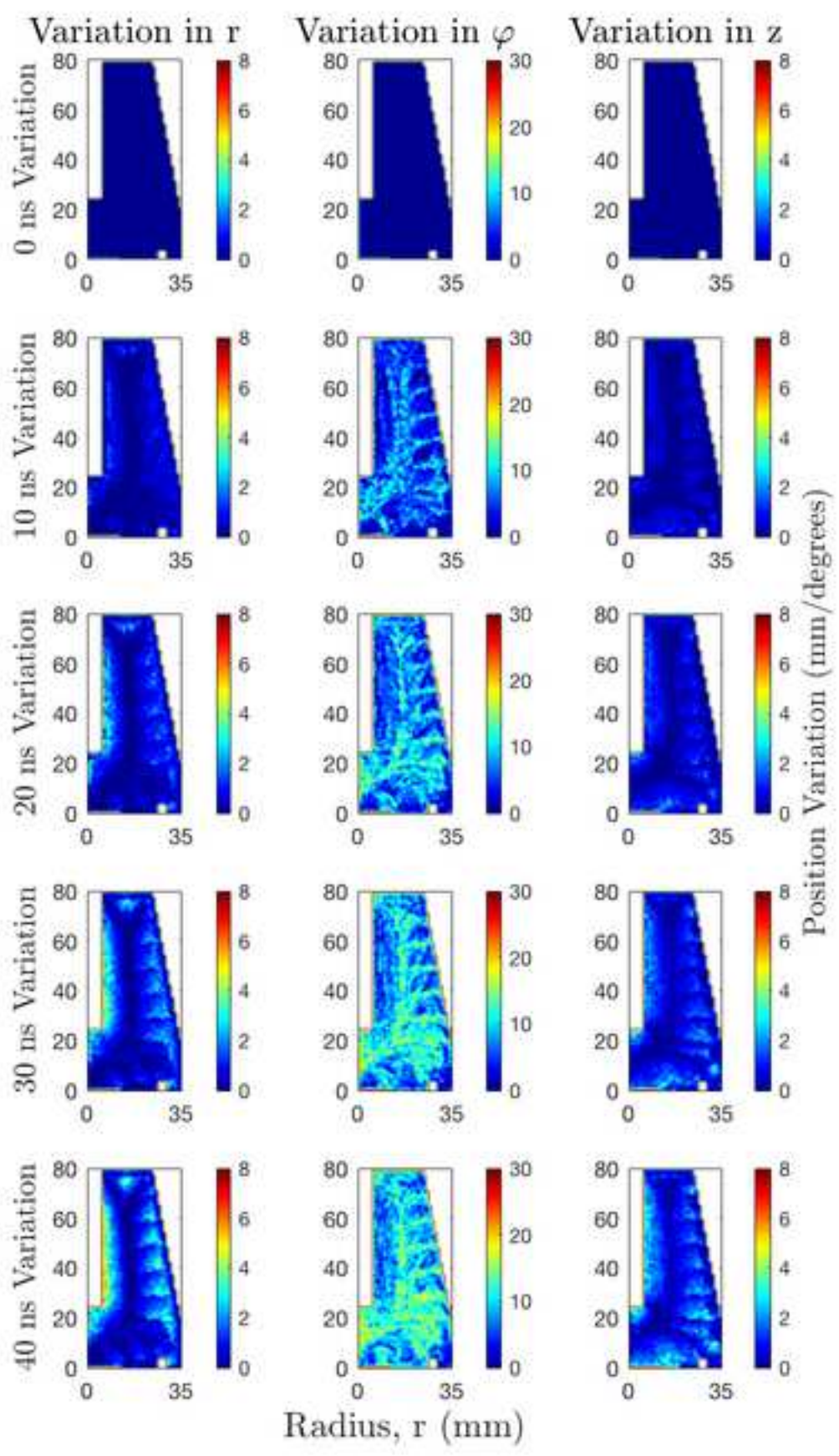


Figure10



Response to reviewers

Reference: NIMA-D-17-01100

Submitted: “Position Resolution Simulations for the Inverted-coaxial Germanium Detector, SIGMA”

Corresponding author: Dr Jonathan Wright

The authors would like to thank the reviewers for providing constructive feedback on the submitted article. We are pleased that reviewer 1 has recommended the work for publication, following a few small modifications. We would like to respond to each of the comments and identify the actions taken to improve the article.

### Reviewer 1:

The first reviewer has provided detailed comments, which have been addressed by the authors:

#### 1 – Page 2 line 27 :

*“One of the benefits of point-contact detector is the reduced capacitance (1 pF) of the electrode when compared to that of standard coaxial detector. It would be more informative to mention the corresponding capacitance value for standard detectors in the manuscript.”*

The only information we have on coaxial detector capacitance has been given in confidence therefore exact values cannot be relayed. To provide scale “(~10’s of pF)” has been added to the text.

#### 2 – Page 2 line 34 :

*“BeGE is not defined while it is done later on, at line 235. Should be corrected.”*

Definition has been removed from line 235 and added to line 34.

#### 3 – Page 3 line 42 :

*“the authors should elaborate more about the location of the position interaction within less than a 1 mm. Is this performance expected with any pulse shape analysis algorithm or with a specific one? If so this should be emphasized.”*

The performance of PSA algorithms will depend upon the variation in signal shapes. The algorithm used for this work was a FoM minimisation technique but the signal variation in SIGMA is what provides the improvement over other HPGe detectors. More advanced algorithms should provide at least the same levels of performance.

#### 4 – Page 3 line 44 :

*“Ref.5 corresponds to in-beam position resolution of AGATA whereas ref.6 is not. I would suggest M. Descovich et al, NIM 533 (2005)535 as the proper reference 6.”*

Reference 6 has been replaced throughout the document.

5 – Page 3 line 58 :

*“the passivation region as mentioned in the text, is not clearly seen in Figure 1. The authors can easily modify the figure to make it clear for the reader.”*

Figure 1 has been altered so that the passivation region is highlighted in blue. Text altered correspondingly to alert the reader to this.

6 – Page 5 line 75 :

*“segments 17&18 ” should correctly written as “segments 17 and 16” ”*  
Corrected.

7 – Page 5 :

*“Ref 7 and 8 correspond to the same web page link and hence should be merged into a single reference.”*

Corrected.

8 – Page 6 line 93-94 :

*“The operational voltage as measured by the manufacturer is NOT slightly higher compared to simulated full depletion. The authors should rephrase this sentence and elaborate more regarding about the difference of 1000 Volts.”*

We agree that this sentence was phrased in a confusing manner and have therefore reworded it.

9 – Page 7 line 105 :

*“miss-spelling of upto -> up to”*  
Corrected.

10 – Page 8 :

a) *“Fig4 shows two examples of point contact pulses for the chosen interaction points. To be consistent with Reference 1, the authors should/could also display the outer segment and core contact pulses. In addition, it is stated that due to the sharp rising edge, it is much easier to differentiate multiple interactions than in a comparable coaxial detector. Is this statement valid for any position of the interactions? If one chooses a very close interactions points near the green or the red circles, how does the super pulse change?”*

b) *Figure5 shows an example of full trace and it is not clear whether it corresponds to the interactions that are displayed in Fig4. In addition, Fig5 displays a signal distortion around segment 8 that I don't understand. Could the authors elaborate on that?”*

c) *At line 144, the difference in pulse quality is pointed out but I don't see any comparison with another super pulse (for example when using an AGATA crystal) that illustrates this quality.”*

- a) The purpose of Figure 4 is to illustrate the temporal variation in the point contact pulse as a function of position which does not require the core and outer segment pulses. Examples of pulses from all segments are shown in Fig 5.

For nearby interactions, a superposition will occur in the point contact trace however the drift time varies significantly over short distances; thus enabling the two pulses to be identifiable. The two pulses in Figure 4 were chosen so this effect was clearly visible to the naked eye and not just identifiable through computer based analysis.

- b) The full trace shown in Figure 5 is for a multi site event, i.e. a single photon that has scatter multiple times within the crystal, whereas the interactions in Figure 4 are singles used to illustrate the temporal variation in the point contact trace as a function of position. They do not correspond to the interaction positions shown in red and green. The signal distortion in segment 8 is likely a result of multiple charge carriers from the multiple interactions (2 x scatter + PE absorption) drifting in opposite directions through the weighting potential of segment 8. The same effect is seen in all segments to varying degrees, however the larger induced charges dilute the visibility of this to the naked eye.
- c) Added a reference to *S.Akkoyun et al., NIM A668(2012)26* where example pulses are presented.

11 – Page 10 :

*“Figure 8 as an extension of the results of Fig.6 is not clear and the final collecting electrode versus the position of the interaction is not obvious for a general reader. I would suggest an improvement of this section together with a correction of typos than one sees on the labels of Fig.8.”*

The section has been reworded to make it more accessible to a general audience as described below. The label on Fig.8 has been corrected.

**Original:**

To understand the drift paths of the electrons in this detector, the final collecting electrode of the electron is plotted as a function of  $\gamma$ -ray interaction position in Figure 8. This plot is an extension of the results in Figure 6 providing a clearer image of the relative influence of each electrode on charge collection path. The scale of the core contact is clear to see, with most interactions occurring near the central axis of the crystal terminating the core. However for interactions occurring far from the central axis of the detector, there are clearly defined bands representing each of the outer contacts.

**New:**

To understand the drift paths of the electrons in this detector, the electron collecting electrode, outer hit segment, is plotted as a function of  $\gamma$ -ray interaction position in Figure 8. The relative sizes of each of the segments in Figure 8 are a direct result of the relative strengths of the weighting potentials shown in Figure 6 and provide a clearer image of the relative influence each electrode has on the charge collection path. The scale of the

core contact is clear to see, with most interactions occurring near the central axis of the crystal terminating the core. However for interactions occurring far from the central axis of the detector, there are clearly defined bands representing each of the outer contacts.

12 – Page 10 line 186 :

*“references should be added for the performance of gamma-ray tracking versus the accurate measurements of the interaction point positions and energies.”*

Added reference to *G.J. Schmid, et al., NIM A430(1999)69-83* which explains the effects of both energy and positions resolution on the performance of a tracking algorithm used for GRETA. More specifically, this paper explains how the errors in the position and energy of the gamma-ray corresponds to the errors in the individual parameters used in the tracking algorithm.

13 – Page 10 line 191 :

*“a reference for the grid search algorithm is suitable”*

The grid search algorithm used is a simple exhaustive grid search with all modifications outlined in the text. The FoM minimisation is a standard mathematical procedure.

14 – Page 10 Line 199 :

*“outputted is probably an incorrect word and should be corrected.”*

Changed from “pulses directly outputted by SigGen” to “pulses directly generated from SigGen”

15 – Page 11 line 205 :

*“A grid search algorithm” to be replaced by “A grid search (GS) algorithm” in order to make the reader understanding what is referred to as GS1, GS2 and GS3.”*

Altered.

16 – Page 11 line 209 :

*“ $S^m_{ij}$  being the measured pulses over the number of segments is confusing since all the work presented in this paper is based on simulated data. The authors should correct this.”*

Changed  $S^m$  to refer to modified pulses instead of measured.

17 – Page 12 line 228 :

*“1 mm x 1 mm x 3° grid. I Guess this a 1 mm x 3° x 1 mm grid that corresponds to (r,phi,z). Is a 3 degrees small enough? What one would expect when using 1mm x 1 deg X 1 mm grid basis?”*

That is correct. The effects of using a 1° grid has been investigated and the results showed no statistically significant variation from those presented. This results from the variation in drift time over 3° being less than the drift time variation over 1 mm in R and Z, therefore the gains from a finer phi grid are lost in the errors from the R,Z grid. Given the difference in

computation power required for the smaller grids, it was decided to use the larger grid for the study presented.

18 – Page 12 line 236 and 238 :

*“the authors should choose between a single notation for consistency : either peak-to-peak or Peak-to-Peak in the entire text.”*

Corrected.

19 – Page 13 line 267 :

*“a reference for the PSA should be added unless the authors refer to the GS algorithm.”*

I have added the reference *K.Vetter, et al.,NIM A452(2000)223-238* for the use of PSA as a means of improving position resolution through the use of charge pulses.

20 – Page 14 line 272 :

*“a simple and a more complex  $t_0$  algorithm is not clear and should be explained in more details. Did the authors investigate the effect of applying the Kolmogorov-Smirnov method (EPJA 40(2009)249?)”*

The sentence was ambiguous and has been removed. The method used, as described in the text, worked sufficiently well for this study and provides us with a reference for future work. The method in question was not investigated, however such methods may be looked at when we begin optimising the PSA process and start to analyse experimental data.

21 – Page 16 line 316 :

*“the reference to the mentioned published results is missing.”*

Reference is to AGATA/GRETINA papers discussed earlier. They have been added.

22 – Page 17 line 323 :

*“The comparison of the position resolution as obtained in this work and those obtained with AGATA and GRETINA is not consistent. F. Recchia paper refers to an energy of 1.3 MeV whereas for GRETINA one refers to a 2 MeV line.”*

Added the energies of each study to provide clarity to the reader. It is expected that higher energy signals will produce better performance due to the increased signal-to-noise ratio on the pulses and therefore SIGMA will give at least the quoted values or better if a higher energy study were to take place.

23 – Page 21 line 412 :

*“unit for  $t_0$  is missing”*

*line 417 :*

*“full stop is missing between "1 MeV" and "These values" ”*

Corrected.

24 – Page 21 Table 4 :

*“when using SIGMA in a standalone mode, a tiny difference is seen in the achieved FWHM at 0.5 and 1 MeV (4.54 versus 4.37 mm). However, when SIGMA is used with an ancillary detector indeed one notices the improvement; but one also gets about 50% difference (0.64 versus 0.33 mm): Is there an explanation for this?”*

The effects of the time alignment are much more significant than the effects of the factor 2 change in RMS noise from 1 MeV -> 500 keV. Refer to the results from the RMS and Pulse Alignment studies for confirmation of this.

25 – Conclusion :

*“The conclusion emphasizes the unprecedented position resolution obtained with sigma and such this would help AGATA and GRETA tracking rays improve their performance. If so, what is the current limitation of point contact detector that makes it not usable for AGATA and GRETA yet?”*

As with the AGATA and GRETINA arrays, technical evolution in the manufacturing of novel detectors is required. A prototype n-type detector is currently under investigation, *M.Salathe et. al, NIM A868(2017)19-26*, and the p-type discussed here is currently being manufactured. Once the performance of both detectors are experimentally validated, it is expected they will offer a step change in array performance as predicted by the work in *R.Cooper et. al, NIM A665(2011)25-32* and in this paper.

26 – Figure captions should be revised :

*“For example : Figure 3, the authors should explicitly mention calculated/simulated electric potential and calculated electric field strength. Figure 9-10, the x axis as labelled 10 20 30 is not appropriate.”*  
Corrected.

27 – References :

*“Ref5 : misspelling of F. Recchia  
Ref6 : to be replaced by the suggested one (see above)  
Ref7 and 8 : to be merged in a single reference”*  
Corrected.

**.tex file**

**[Click here to download LaTeX Source Files: SIGMA\\_Modelling.tex](#)**

**.bib file**

**[Click here to download LaTeX Source Files: SIG\\_Mod.bib](#)**